remote sensing

MDPI

Article

Seasonal Variability of the Surface Circulation in the Tyrrhenian Sea: New Insights from SWOT Altimetry and Tide Gauge Records

Laura Fortunato [1,*], Giuseppe Aulicino [1], Maxime Ballarotta [2], Ananda Pascual [3], Giannetta Fusco [1], Berardino Buonocore [1] and Yuri Cotroneo [1,4]

[1] Dipartimento di Scienze e Tecnologie, Università degli Studi di Napoli Parthenope, 80143 Naples, Italy; giuseppe.aulicino@uniparthenope.it (G.A.); giannetta.fusco@uniparthenope.it (G.F.); berardino.buonocore@collaboratore.uniparthenope.it (B.B.); yuri.cotroneo@uniparthenope.it (Y.C.)
[2] Collecte Localisation Satellites (CLS), 31520 Ramonville Saint-Agne, France; mballarotta@groupcls.com
[3] Institut Mediterrani d'Estudis Avançats (IMEDEA), Spanish National Research Council—University of the Balearic Islands (CSIC-UIB), 07190 Esporles, Spain; ananda.pascual@imedea.uib-csic.es
[4] Consorzio Nazionale Interuniversitario per le Scienze del Mare (CoNISMa), 00196 Rome, Italy
* Correspondence: laura.fortunato@phds.uniparthenope.it

Highlights

What are the main findings?

- SWOT-enhanced altimetry provides a finer spatial representation of sea-level gradients and fine-scale surface circulation variability than conventional gridded altimetry.
- High-resolution SWOT observations provide an enhanced representation of frontal structures, coastal jets, and fine-scale mesoscale circulation features across different seasons.

What are the implications of the main findings?

- SWOT provides additional spatial information for the characterization of fine-scale coastal and mesoscale dynamics in semi-enclosed Mediterranean basins.
- The combined use of SWOT altimetry, SST gradients, and tide gauge observations provides complementary insights into seasonal circulation variability and coastal exchanges.

Abstract

The Tyrrhenian Sea plays a key role in Mediterranean circulation. However, the seasonal evolution and coastal circulation patterns of its surface circulation remain only partially resolved by previous observations, particularly at mesoscale and submesoscale. In this study, we investigate the seasonal and coastal variability of Tyrrhenian Sea surface circulation by combining high-resolution wide-swath altimetry from the Surface Water and Ocean Topography (SWOT) mission with conventional multi-mission altimetry, satellite-derived Sea Surface Temperature (SST), and coastal tide gauge observations. Compared to conventional gridded altimetry, SWOT-enhanced products exhibit higher Absolute Dynamic Topography (ADT) gradients, with mean seasonal increases of 4–6% in winter-spring and up to 12–15% in summer-autumn. Surface velocity fields also exhibit generally higher spatial variability (3–10% in most seasons) and stronger mean velocities, with mean seasonal increases of up to 14% relative to conventional gridded altimetry. These differences result in a finer spatial depiction of frontal systems, coastal jets, and mesoscale circulation features. These patterns are consistent with independent tide gauge records and the spatial agreement between altimetry-derived structures and SST frontal gradients in representative seasonal case studies. While confirming the well-known seasonal cyclonic circulation, which is stronger in

Check for updates

Academic Editor: Kaoru Ichikawa

Received: 29 May 2026
Revised: 8 July 2026
Accepted: 11 July 2026
Published: 14 July 2026

Copyright: © 2026 by the authors. Licensee MDPI, Basel, Switzerland. This article is an open access article distributed under the terms and conditions of the Creative Commons Attribution (CC BY) license.

winter-spring and weaker in summer, our results indicate that SWOT-enhanced altimetry offers a more detailed spatial representation of fine-scale coastal and mesoscale circulation features than conventional gridded altimetry. Overall, these findings highlight the potential of SWOT-enhanced altimetry to improve the spatial characterization of Mediterranean upper-ocean circulation and its fine-scale variability, providing a valuable framework for future studies of coastal dynamics and mesoscale processes.

Keywords: Surface Water and Ocean Topography (SWOT); Tyrrhenian sea; satellite altimetry; sea surface height; coastal circulation; tide gauges; sea surface temperature

1. Introduction

The Tyrrhenian Sea (TYS, hereafter) is the deepest basin of the western Mediterranean Sea and has long been recognized as an area of considerable oceanographic interest [1,2]. Its circulation is shaped by interactions among multiple water masses, wind forcing, and marked seasonal variability across a range of spatial and temporal scales [3–5], contributing significantly to the thermohaline functioning of the Mediterranean Sea [6,7]. Beyond its scientific relevance, the TYS hosts ecologically important habitats and supports important socio-economic activities, including fisheries and maritime transport [8,9].

Despite the recent expansion of in situ observing platforms, such as gliders and Argo floats, satellite altimetry remains essential for monitoring ocean surface circulation over regional to basin scales [10,11]. However, conventional nadir altimetry products are limited by their spatial resolution, which restricts their ability to capture detailed circulation patterns, particularly in semi-enclosed basins such as the TYS [12].

As a result, the contribution of mesoscale and submesoscale processes to coastal exchanges, frontal dynamics, and seasonal circulation variability may be underestimated.

Multi-mission altimetry products have partially mitigated these limitations by improving coverage and accuracy, but further advances are required to capture the full complexity of the seasonal surface circulation [13,14]. Nevertheless, their effective spatial resolution remains insufficient to fully resolve coastal jets, frontal instabilities, and fine-scale variability.

The Surface Water and Ocean Topography (SWOT) mission represents a significant technological leap forward, providing wide-swath, high-resolution measurements that enable a more detailed representation of surface circulation than conventional nadir altimetry [15–17]. This capability offers new opportunities to deepen our understanding of surface circulation variability in regional seas [18–22].

In this study, we examine the seasonal surface circulation of the TYS by comparing the first available data from the SWOT-enhanced altimetry products with conventional multi-mission datasets. Therefore, we aim to (i) quantify the added value of SWOT in improving the spatial representation of mesoscale and finer-scale circulation features using metrics such as Absolute Dynamic Topography (ADT) gradients and geostrophic surface velocity fields, (ii) assess its capability to characterize coastal jets and frontal structures across seasonal regimes, and (iii) evaluate the consistency of these features with independent tide gauge and Sea Surface Temperature (SST) observations.

Beyond the methodological comparison, this study provides one of the first integrated assessments of SWOT-enhanced altimetry in a semi-enclosed Mediterranean basin by relating high-resolution surface height gradients to independent observations of coastal sea-level variability and surface thermal structure.

Although previous studies have described the large-scale circulation of the TYS using conventional satellite altimetry, the seasonal evolution of coastal jets, frontal structures, and

finer-scale mesoscale variability remains only partially resolved because of the effective spatial resolution of traditional gridded products. Furthermore, the capability of the new SWOT-enhanced products to improve the representation of these features in a semi-enclosed Mediterranean basin has not yet been systematically assessed.

The present work provides a quantitative and observationally constrained framework to assess differences in the representation of seasonal surface circulation features between SWOT-enhanced and conventional altimetry, and their agreement with independent observations.

The paper is organized as follows: Section 2 describes the study area. Section 3 presents the datasets and methodology, including the satellite altimetry, tide gauge, and SST observations. Section 4 presents the results, focusing on the comparison between conventional and SWOT-enhanced altimetry products and their consistency with independent observations. Finally, Section 5 discusses the main findings and limitations of the study, while Section 6 presents the conclusions.

2. Study Area

The Tyrrhenian Sea (TYS, hereafter) is a semi-enclosed basin of the western Mediterranean Sea, bordered by the Italian Peninsula to the east, the islands of Sardinia and Corsica to the west and northwest, and Sicily to the south (Figure 1a). Covering about 231,000 km^2 and reaching a maximum depth of 3785 m in its central plain [23], it is considered the most isolated basin of the western Mediterranean Sea [1].

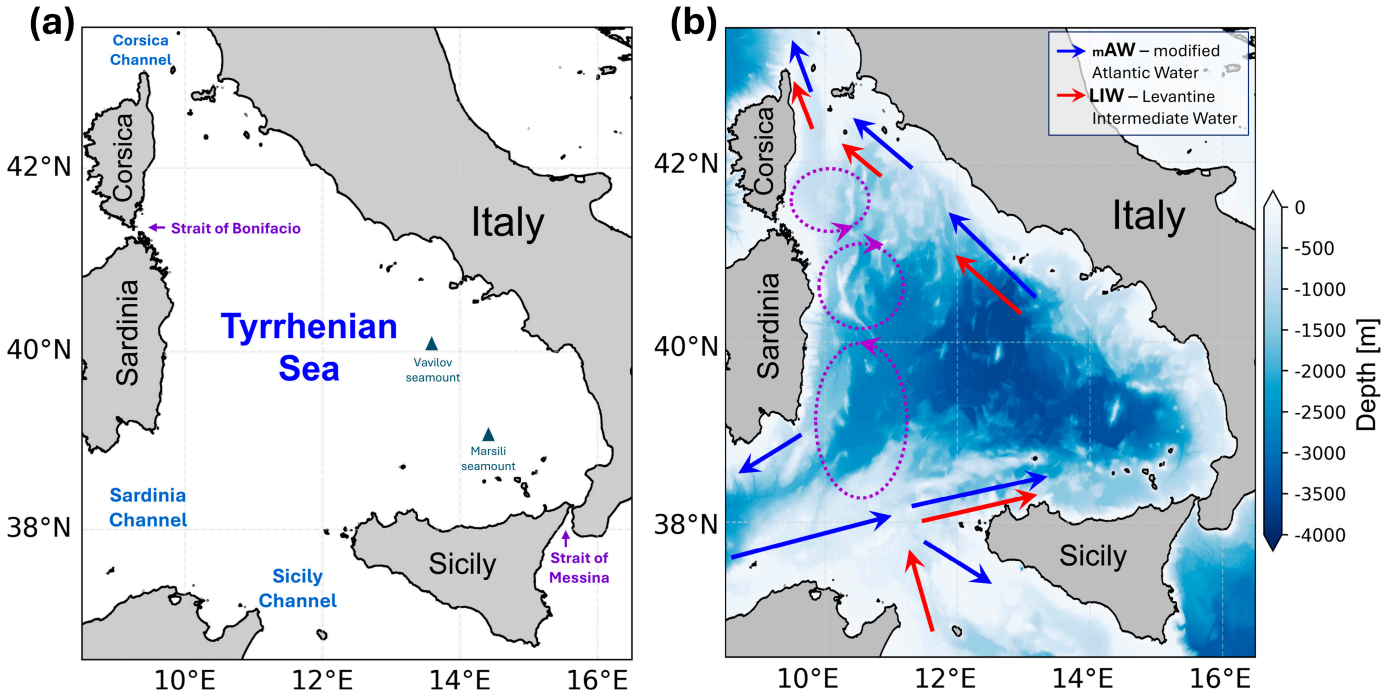


Figure 1. (**a**) Map of the Tyrrhenian Sea showing its main topographic features, including straits, channels, and seamounts. (**b**) Bathymetric map of the basin. Arrows indicate the main pathways of surface-modified Atlantic Water (mAW, blue) and intermediate Levantine Intermediate Water (LIW, red). Purple ovals represent the quasi-permanent Bonifacio dipole and the cyclonic circulation between Sardinia and Sicily, two distinctive features of the TYS basin-scale circulation. Adapted from [24].

The TYS plays a key role in the Mediterranean thermohaline circulation [6,7], contributing to the formation and redistribution of dense water masses whose properties have shown marked variations over recent decades [4,25,26]. The TYS bathymetry is complex,

with a deep central plain surrounded by steep continental slopes and prominent seamounts and ridges, including the Vavilov and Marsili seamounts, which significantly influence local circulation and mixing processes [24,27]. The basin exchanges water with adjacent sub-basins through three major openings: the Corsica Channel to the north, the Sardinia Channel to the southwest, and the Sicily Channel to the south. Additionally, smaller but dynamically important passages, the Strait of Bonifacio between Corsica and Sardinia, and the Strait of Messina between Sicily and mainland Italy, further modulate water exchanges and circulation pathways.

Circulation within the TYS results from interactions among different water masses and forcing mechanisms [28] (Figure 1b). In the upper layer (100–200 m), modified Atlantic Water (mAW), identified by a subsurface salinity minimum ($S < 37.4$), enters the basin primarily along the northern coast of Sicily [29,30]. At intermediate depths, the salty ($S > 38.5$) Levantine Intermediate Water (LIW) arrives from the eastern Mediterranean through the Strait of Sicily and undergoes transformation and mixing within the basin [31,32]. The deepest layers are filled by Western Mediterranean Deep Water (WMDW), characterized by lower potential temperature ($\theta < 13\ ^{\circ}C$) and salinity ($S < 38.5$), which enters through deep passages between Sardinia and Sicily. Mixing between LIW and WMDW below 1000 m forms Tyrrhenian Deep Water (TDW), a distinct water mass that contributes to the basin's thermohaline structure [2,7,33]. A locally formed Tyrrhenian Intermediate Water (TIW) develops between 100 and 200 m during winter convection and is associated with the basin-scale cyclonic circulation and the Bonifacio gyre [24,27].

The interaction of these water masses with bathymetry, wind forcing, and buoyancy fluxes produces a circulation pattern with marked seasonal changes [27]. During winter and spring, the basin exhibits a well-developed cyclonic circulation extending from the surface to intermediate depths. The mAW enters along the northern coast of Sicily. Part of the flow recirculates near the southern opening, while the remainder progresses northward toward the Corsica Channel. A fraction continues into the Ligurian Sea, while the remainder loops back southward, feeding a persistent cyclonic gyre east of the Bonifacio Strait. LIW generally follows the western margin of the basin, exiting mainly through the Sardinia Channel. Wind forcing is generally associated with the reinforcement of the dipole structure near the Bonifacio Strait and a broader cyclonic flow along the Campanian coast [6,34,35].

In summer, increasing stratification isolates the basin from surrounding Mediterranean waters through strong thermohaline fronts [3,36]. The large-scale cyclonic cell weakens, and both mAW and LIW tend to recirculate within the basin, with minimal outflow through the Corsica Channel. Circulation becomes more fragmented, with mesoscale eddies and coastal jets persisting for longer periods but exhibiting reduced kinetic energy. Additional eddies have been reported to develop in the eastern TYS, enhanced by stratified conditions and weaker basin-scale flow [33]. By autumn, the TYS enters a transitional phase. Summer stratification persists in the upper layers but increasing wind activity and shifting buoyancy fluxes enhance vertical mixing. This gradual weakening of the summer structure re-intensifies the cyclonic circulation, progressively re-establishing the winter-spring configuration. Below the surface, the TYS exhibits a vertically stepped thermohaline structure, commonly referred to as thermohaline "staircases", resulting from the superposition of distinct water masses of different origin and properties [28,37]. These layers reflect the coexistence of mAW in the upper 100 m, TIW at intermediate depths, and the saltier LIW below [2,38,39]. Staircases are associated with double-diffusive convection processes that generate alternating well-mixed layers and sharp interfaces, which can persist over long timescales and significantly influence vertical mixing and heat-salt fluxes within the basin. Recent observations indicate that such thermohaline staircases are a permanent and dynamically active feature of the TYS [28,37]. In the present study, we specifically focus on

the surface circulation, as inferred from satellite altimetry observations, which are most sensitive to upper-ocean dynamics.

3. Materials and Methods

To investigate the seasonal variability of surface circulation in the TYS, we used three satellite altimetry datasets covering the year 2024.

The conventional multi-mission gridded product and the SWOT-enhanced gridded field are compared within a quantitative framework to evaluate differences in the representation of surface dynamics. In addition, the SWOT Level-3 (L3) product is analysed independently and is not included in the gridded-product intercomparison.

In situ sea-level observations from coastal tide gauges are used as an independent reference to validate the temporal variability of Sea Surface Height Anomaly (SSHA). SST observations are used as a proxy for frontal activity and are not involved in circulation reconstruction.

The gridded altimetry products are compared in a non-merged framework, in which each dataset is analysed independently using a common set of circulation diagnostics. This approach provides an objective comparison to assess the potential of SWOT-enhanced products relative to conventional altimetry while avoiding cross-product contamination.

3.1. Satellite Altimetry

Altimetry provides estimates of Absolute Dynamic Topography (ADT) and geostrophic velocities, supporting the characterization of mesoscale to seasonal circulation regimes. The combination of gridded and swath-based altimetry provides complementary information on basin-scale circulation and fine-scale coastal dynamics across seasons.

All datasets are analysed using a consistent set of circulation diagnostics based on SSHA, ADT, and the geostrophic velocity components provided by each product, without any additional derivation from Sea Surface Height (SSH) gradients. Native land–sea masks provided with each dataset were retained throughout the analysis, and no additional coastal masking was applied.

- The first dataset is the ***European Seas Gridded Level-4 (L4) Sea Surface Heights and Derived Variables NRT*** product (SEALEVEL_EUR_PHY_L4_NRT_008_060, https://doi.org/10.48670/moi-00142), dataset release 202311, covering the period from 1 January 2024 to 25 November 2024. The dataset was accessed in June 2025. Developed within the DUACS (Data Unification and Altimeter Combination System) framework, it provides daily optimally interpolated fields of Sea-level Anomaly (SLA) over the European Seas on a $1/8^\circ \times 1/8^\circ$ spatial grid, referenced to the 1993–2012 climatological period. The product is generated through Optimal Interpolation (OI) [40] by merging observations from multiple altimeter missions, including TOPEX/Poseidon (TP), Jason series (Jason-1 (J1) and OSTM/Jason-2 (J2)), ERS-1, ERS-2, ENVISAT (EN), Geosat Follow On (GFO), Cryosat-2 (C2), Saral/AltiKa (AL), and Haiyang-2A (HY-2A), providing consistent, high-quality fields for regional applications in European waters. The dataset is distributed by the Copernicus Marine Service (CMEMS).
- The second dataset is the ***Experimental multimission gridded L4 sea-level heights and velocities with SWOT*** product (https://doi.org/10.24400/527896/A01-2024.007), version 2.0.1, covering the SWOT Science Phase from 1 January 2024 to 25 November 2024. The dataset was accessed in June 2025. This dataset is derived from Level-3 (L3) along-track altimetry, combining measurements from conventional nadir missions (Jason-3, CryoSat-2, Saral/AltiKa, Sentinel-3A/B, Sentinel-6A, HaiYang-2B) with SWOT nadir and KaRIn observations (https://doi.org/10.24400/527896/A01-2023.018). Fields are produced using the MIOST (Multiscale Interpolation of Ocean Surface Topog-

raphy) approach [41–43], which explicitly accounts for different dynamical modes (e.g., geostrophic, barotropic, equatorial wave processes) by constructing independent covariance components. This method is designed to provide a more detailed reconstruction of mesoscale and finer-scale structures, which makes the product suitable for assessing the added value of SWOT observations. The dataset provides daily fields at a $1/8^\circ \times 1/8^\circ$ resolution and is distributed by AVISO (SSALTO/DUACS, CNES).

- The third altimetry dataset is the ***SWOT Expert Level 3 Low-Rate Sea Surface Height*** (L3_LR_SSH_Expert) product (https://doi.org/10.24400/527896/A01-2023.018), version 3.0. The dataset was accessed in October 2025. Only selected acquisition dates, corresponding to the SST case studies presented in this work, were analysed. In this work, we used the most recent release, version 3.0, made available by AVISO+/DUACS in 2025. This new version includes an updated reprocessing of the 2 km basic and expert products and introduces several improvements with respect to v2.0.1, including enhanced geophysical corrections, revised algorithms, and consistency with the reduced-latency Level-2 inputs. The v3.0 processing chain now operates with a target latency of ~48 h, enabling near-real-time applications and improved compatibility with operational oceanography systems. The Expert L3 product provides high-resolution gridded ocean topography fields over the KaRIn swath, including Sea Surface Height Anomaly (SSHA), Mean Dynamic Topography (MDT), Mean Sea Surface (MSS), geostrophic velocities (absolute and anomaly components), backscatter (sigma0), quality flags, and all standard altimetric corrections, supplemented by updated external model fields. Data are mapped onto a ~0.05° (~5 km) regular grid, offering a detailed representation of mesoscale and submesoscale variability, though spatial coverage remains confined to the KaRIn swath. The dataset is produced by AVISO+/DUACS within the DESMOS Science Team framework and is specifically designed to exploit the full capabilities of the SWOT KaRIn instrument.

Hereafter, the three satellite altimetry datasets will be referred to as: DUACS-OI for the near-real-time gridded L4 product (SEALEVEL_EUR_PHY_L4_NRT_008_060); MIOST-K for the experimental gridded L4 product incorporating SWOT KaRIn data; and SWOT L3 for the expert SWOT Level-3 ocean product.

In particular, the DUACS-OI product is based on optimal interpolation (OI) of along-track nadir altimetry measurements. In contrast, the MIOST-K product combines conventional nadir altimetry with SWOT KaRIn wide-swath observations within a multiscale reconstruction framework. Therefore, the comparison reflects differences in both the observing system and the data reconstruction methodology.

Satellite Altimetry Data Processing

The three altimetry products are not merged but analysed independently to preserve their native resolution characteristics. DUACS-OI is considered the reference multi-mission product, while MIOST-K provides a dynamically consistent multi-scale reconstruction that incorporates SWOT observations. SWOT L3 is used independently and is not included in the gridded product intercomparison nor in any seasonal composite analysis. Comparisons between DUACS-OI and MIOST-K are performed over identical spatial domains and temporal sampling windows, using seasonal mean fields derived from daily data averaged over standard climatological seasons (winter: DJF, spring: MAM, summer: JJA, autumn: SON).

To provide an objective comparison between the two L4 products, several spatial metrics were calculated from the seasonal mean fields, including mean surface velocity, mean ADT gradient magnitude, minimum and maximum ADT anomaly, and the spatial standard

deviation of velocity magnitude. Relative differences between MIOST-K and DUACS-OI were expressed as percentage changes using DUACS-OI as the reference dataset.

The geostrophic velocity magnitude was calculated as:

$$V = \sqrt{u^2 + v^2} \tag{1}$$

where u and v are the geostrophic velocity components provided by each dataset.

The *ADT* gradient magnitude was calculated as:

$$|\nabla ADT| = \sqrt{\left(\frac{\partial ADT}{\partial x}\right)^2 + \left(\frac{\partial ADT}{\partial y}\right)^2} \tag{2}$$

where *ADT* is the Absolute Dynamic Topography, and x and y represent the zonal and meridional directions, respectively. Spatial derivatives were estimated using finite differences on the native grid fields, with horizontal grid spacing converted from degrees to metres using a standard Earth-radius-based approximation.

Mean values and standard deviations were calculated over all valid ocean grid cells within the common analysis domain, while minimum and maximum ADT values were extracted from the seasonal mean fields.

The primary analysis presented in this study focuses on the two gridded L4 altimetry products (DUACS-OI and MIOST-K), which provide spatially continuous daily fields suitable for basin-scale and seasonal analyses.

Although the MIOST-K product incorporates SWOT observations, it remains a mapped product and therefore reflects the characteristics and limitations of the underlying interpolation methodology. Consequently, the present study primarily assesses the added value of SWOT-enhanced gridded altimetry rather than the full observational capability of the native SWOT KaRIn measurements. Given the deterministic nature of the product intercomparison, the reported percentage differences are intended as descriptive metrics of the relative differences between the products. Accordingly, no formal statistical significance or uncertainty analysis was performed.

The SWOT L3 product is not included in any of the quantitative analyses or seasonal composites and is used exclusively as an independent qualitative reference in selected case studies, where its native swath structure is visually compared with SST and altimetry fields to support the interpretation of mesoscale features. This approach provides a clear separation between quantitative evaluation (L4 products) and qualitative consistency checks (L3 observations).

3.2. Tide Gauge Data

We used sea-level records from tide gauges along the boundaries of the TYS to describe coastal sea-level variability during 2024 (Figure 2a). Additionally, the temporal consistency between tide gauge observations and satellite products was used to assess the consistency of satellite-derived sea-level fields. Tide gauge records are used exclusively as an independent reference for temporal sea-level variability and are not interpreted as direct measurements of ocean circulation.

The first dataset consists of sea-level measurements from a "Thalimedes" tide gauge (OTT HydroMet) installed in 2002 in the main harbour of Ischia Island (Gulf of Naples; 40.7458°N, Lon: 13.9405°E) by the Department of Science and Technology (DIST) of the University of Naples Parthenope. The tide gauge operates inside a stilling well and measures water level using a float system, referenced to benchmarks placed on the dock. The instrument records sea level at 5 min intervals and has remained stationary throughout the

study period. Regular maintenance is conducted every six months to ensure measurement accuracy [44].

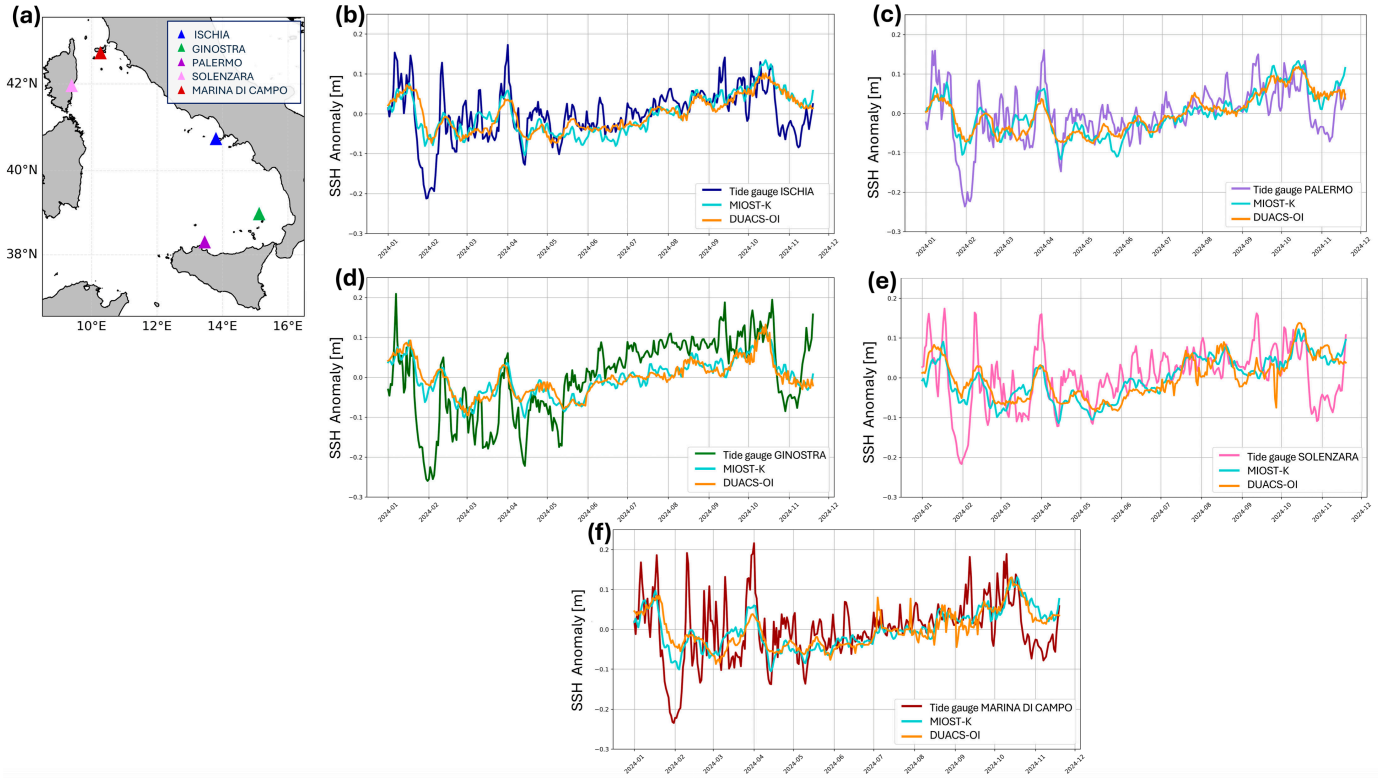


Figure 2. (**a**) Locations of the tide gauges used in this study along the Italian and Corsican coasts. Comparison of tide gauge Sea Surface Height anomalies with MIOST-K (cyan) and DUACS-OI (yellow) sea surface height anomalies at five coastal stations in the Tyrrhenian Sea: (**b**) Ischia, (**c**) Palermo, (**d**) Ginostra, (**e**) Solenzara, and (**f**) Marina di Campo.

Additional sea-level data were obtained from the Istituto Superiore per la Protezione e la Ricerca Ambientale (ISPRA) National Tide Gauge Network (Rete Mareografica Nazionale, RMN), including the stations in Ginostra (38.7852°N, 15.1908°E), Palermo (38.1214°N, 13.3713°E), and Marina di Campo (42.7426°N, 10.2383°E). These stations, typically located in port facilities, acquire automatic, real-time sea-level and meteorological observations. Each RMN station is equipped with a primary radar level transducer (microwave sensor) and a secondary float-operated sensor for redundancy and calibration purposes. The radar sensor measures sea level with ±1 mm accuracy and 0.5 mm sensitivity, while the float system has ±1 cm accuracy and 1 mm sensitivity. Both sensors are referenced to benchmarks tied to the Italian high-precision leveling network (IGM) and available in real time via www.mareografico.it. RMN stations record sea level every 10 min and continuously transmit data in real time via industrial UMTS/4G routers.

In addition, we included data from the Solenzara tide gauge (Corsica, France; 41.8583°N, 9.4025°E; station ID: 3177), situated in the main harbour of Solenzara, a town on the eastern coast of Corsica. This station is part of the SONEL (Système d'Observation du Niveau des Eaux Littorales) network, which provides harmonized sea-level measurements along the French coastline. The Solenzara station offers valuable historical data, contributing to the understanding of sea-level variations in the region. The data from this station were accessed through the SONEL database (https://www.sonel.org) and were quality-controlled to ensure consistency and reliability.

Tide gauge measurements provide point-scale observations of sea-level variability, influenced by tidal, meteorological, and oceanographic processes. While they do not

directly resolve surface circulation patterns, they provide a robust reference for evaluating temporal variability in coastal sea level and for assessing the consistency of satellite-derived sea-level anomalies.

All tide gauge time series were first subjected to a linear detrending to remove long-term variability and focus on sub-seasonal to seasonal signals. A basic quality control procedure is then applied to remove erroneous measurements, including physically unrealistic values and isolated outliers. Spikes were identified using a median-based filtering approach, whereby observations exceeding a threshold defined by a multiple of the local median absolute deviation are removed. Data gaps shorter than a few consecutive samples were linearly interpolated to obtain continuous daily time series, after which all records were averaged to a daily temporal resolution to ensure consistency with satellite altimetry products.

No tidal or atmospheric corrections (e.g., Dynamic Atmospheric Correction, DAC) were applied to maintain consistency with the sea-level anomaly definition used in the altimetry datasets. In particular, the omission of tidal correction ensures that both in situ and satellite observations retain a comparable reference level, since tidal signals are not explicitly removed from the altimetry-derived sea-level anomaly fields used in this study. Similarly, atmospheric pressure effects are not removed to avoid introducing external model-based corrections that are not consistently applied across all datasets.

This ensures a consistent definition of sea-level anomalies between in situ and satellite observations, avoiding the introduction of heterogeneous atmospheric corrections across datasets and enabling a more direct comparison of relative sea-level variability.

Moreover, since the analysis focuses on daily averaged time series and seasonal to sub-seasonal variability, the impact of high-frequency tidal and atmospheric signals is expected to be limited and does not significantly affect the robustness of the comparison. Similar approaches have been adopted in previous Mediterranean studies, where minimally processed tide gauge records were used to assess sea-level variability at synoptic to seasonal scales [45–47].

For each station, the nearest altimetry grid point is used for the comparison. The distance between tide gauge stations and the nearest altimetry grid point ranges from 3.05 to 8.33 km, which is within the typical range used in coastal altimetry studies [48].

To assess temporal consistency between tide gauge observations and the L4 altimetry products, a cross-correlation analysis was performed for each station and dataset. The highest correlations were consistently obtained when the altimetry time series were shifted forward by 3 days relative to the tide gauge records. Following this temporal alignment, Pearson correlation coefficients increased by an average of ~0.23 for MIOST-K and ~0.27 for DUACS-OI across all stations. Complete station-by-station Pearson correlation coefficients before and after the temporal alignment are reported in Table S2.

This statistically derived lag is interpreted as resulting from temporal smoothing, space-time mapping, and the reduced effective resolution of L4 gridded altimetry products, rather than representing a physical propagation signal. The optimal lag was subsequently applied only for the statistical comparison and should not be interpreted as a physical propagation time between the two datasets.

Similar temporal mismatches between in situ and gridded altimetry datasets have been reported in previous coastal altimetry studies [47,49,50].

Overall, the in situ observations provide robust coastal sea-level records, supporting the evaluation of both conventional multi-mission and SWOT-enhanced altimetry. The use of correlation and RMSE metrics provides a first-order assessment of the ability of satellite products to reproduce observed temporal variability in coastal sea level.

3.3. Sea Surface Temperature Data

To complement the analysis of altimetry-derived circulation, we used satellite-based SST products provided by the CMEMS. In particular, we used the ***Mediterranean Sea—High Resolution L3S Sea Surface Temperature Reprocessed dataset*** (SST_MED_PHY_L3S_MY_010_042, https://doi.org/10.48670/moi-00314). This product provides a consistent and homogeneous SST time series for the Mediterranean Sea, specifically designed for climate and oceanographic applications. SST fields are used as an independent qualitative diagnostic of surface frontal activity and are compared qualitatively with ADT gradients to assess the physical consistency of detected structures.

The dataset consists of daily nighttime "foundation SST" fields, defined as temperatures largely free of diurnal variability, on a regular $0.05^\circ \times 0.05^\circ$ grid. It merges multi-sensor Level-3 collated observations (L3C) from infrared radiometers such as AVHRR, SLSTR, and VIIRS into super-collated (L3S) fields, using bias correction, cloud-screening, and advanced quality-control procedures. The product is based on the ESA Climate Change Initiative (CCI) climate data record (up to 2021) and is extended from 2022 onwards by the corresponding Interim Climate Data Record (ICDR), ensuring near-real-time continuity and consistency [51,52].

In this study, SST fields were used as an independent qualitative diagnostic of surface thermal variability and frontal activity, and not as direct validation of ocean currents or circulation patterns derived from altimetry. SST gradients were qualitatively compared with corresponding ADT fields from DUACS-OI and MIOST-K to assess the consistency of surface thermal and sea-level structures.

Representative SST scenes with minimal residual cloud contamination (as provided after product-level cloud screening and further verified through visual inspection) were selected for each season (January, April, July, and October) to ensure adequate spatial coverage of the TYS and to minimize cloud-related artefacts. For each selected SST scene, the corresponding SWOT overpass information (cycle and track) and acquisition details are summarized in Table 1. The resulting SST gradients are compared with ADT fields from both MIOST-K and DUACS-OI products corresponding in space and time.

Table 1. Summary of selected SST scenes and corresponding SWOT acquisition cycles and tracks used for the SST-altimetry intercomparison.

Season	Date	SWOT Cycle	SWOT Track
Winter	12 January 2024	9	236
Spring	4 April 2024	13	208, 223
Summer	18 July 2024	18	236, 251
Autumn	30 October 2024	23	236

4. Results

This study provides a quantitative characterization of the dominant circulation regimes in the TYS and their seasonal variability. Particular attention is given to mesoscale and finer-scale features, including cyclonic and anticyclonic eddies, coastal currents, and frontal structures, and their representation across different altimetry products. Additionally, this work assesses how satellite products differ in resolving fine-scale oceanographic structures.

The results are organized across independent datasets. Tide gauge sea-level records are first used as an independent reference to quantify coastal sea-level variability and to support the satellite-derived ADT fields. The seasonal surface circulation patterns are then examined by comparing DUACS-OI multi-mission altimetry with the MIOST-K product, highlighting differences in the representation of finer-scale oceanographic structures, particularly in coastal and boundary current regions. Finally, satellite-derived

SST maps are employed to provide a complementary thermal perspective and to further support the dynamical interpretation of the identified circulation features.

4.1. Coastal Sea-Level Variability from Altimetry and Tide Gauges

Comparison with tide gauge observations indicates that MIOST-K generally shows better agreement with coastal SSHA than DUACS-OI across the TYS (Figure 2). At Ischia (Figure 2b), the Pearson correlation between tide gauge and MIOST-K reaches 0.622 (good), with a Root Mean Square Error (RMSE) of 0.052 m, compared to 0.551 correlation (moderate) and 0.055 m RMSE for DUACS-OI. Similar results are obtained at Palermo (Figure 2c), where MIOST AVISO+ reaches a good correlation of 0.644 and an RMSE of 0.053 m, again showing better agreement than DUACS-OI (moderate correlation 0.593, RMSE 0.058 m). At Ginostra (Aeolian Islands, Figure 2d), MIOST-K achieves the highest skill (good correlation 0.671, RMSE 0.077 m), whereas DUACS-OI remains moderately correlated (0.563, RMSE 0.084 m). At northern sites, performance slightly decreases. For instance, at Solenzara (Figure 2e), the correlation is 0.494 (moderate) for SWOT versus 0.398 (weak to moderate) for DUACS-OI, with RMSEs of 0.065 and 0.071 m, respectively. At Marina di Campo (Figure 2f), MIOST-K reaches a correlation of 0.580 (moderate-to-good) with an RMSE of 0.062 m, compared to 0.450 (moderate) and 0.069 m for DUACS-OI.

To quantify the impact of the 3-day lag correction, correlations between tide gauge and altimetry time series were also computed before temporal alignment. The application of the lag improves the agreement across all stations and both altimetry products.

Overall, the MIOST-K product shows higher correlations and slightly lower RMSE values across all tide gauge stations, although the improvements remain moderate.

Visual inspection is consistent with these statistics, with MIOST-K generally reproducing both the seasonal cycle and the timing and amplitude of energetic short-term anomalies. DUACS-OI tends to underestimate peaks and smooth rapid oscillations, particularly during winter and autumn, where high-frequency mesoscale and finer-scale variability is strongest. Beyond the site-by-site performance, tide gauge records display a coherent temporal evolution, with consistent phases and anomaly timing across the Tyrrhenian stations. This cross-site agreement indicates the consistency of the in situ coastal sea-level signal, helping to distinguish true physical variability from local noise.

The altimetry datasets, although improved with SWOT, generally smooth short-lived and energetic sea-level peaks, reflecting the inherent filtering applied to derive geostrophic SSHA and the limited ability of gridded products to resolve rapid barotropic responses to local atmospheric forcing. A slight seasonal imprint is also evident, with both MIOST-K and DUACS-OI tending to underestimate winter-autumn variability, likely associated with unresolved density-driven and wind-driven processes in narrow coastal zones. At all stations, a pronounced and coherent decline in sea level during November 2024 is clearly evident from tide gauge data. This basin-wide signal is only partially captured by both altimetry products, which correctly reproduce its onset but underestimate its amplitude. Across all sites, MIOST-K shows consistently higher correlations and lower RMSE values, suggesting an improved representation of coastal SSHA relative to DUACS-OI. Overall, the comparison with tide gauge observations suggests that MIOST-K provides a more consistent representation of coastal sea-level variability across the investigated stations.

4.2. Seasonal Surface Circulation

4.2.1. Winter Circulation

During winter, both altimetry products consistently show the well-documented cyclonic circulation that dominates the TYS (Figure 3). Along the Italian coast, a northward-flowing current is observed, extending from the Strait of Sicily to the northern TYS and

partially exiting through the Corsica Channel. This boundary flow is consistent with sea-level anomalies recorded at tide gauge stations, where elevated coastal sea levels are observed during periods of intensified northward flow (Figure 3).

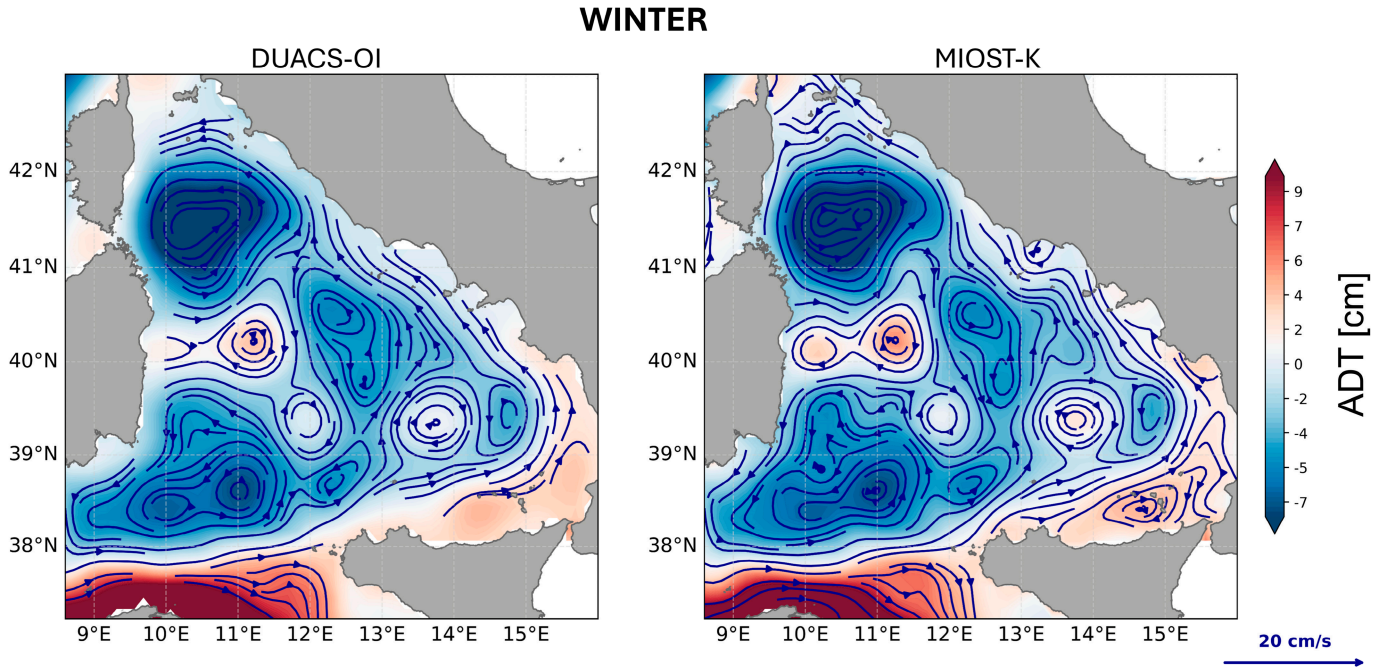


Figure 3. Seasonal mean Absolute Dynamic Topography (ADT) and geostrophic velocity fields for winter in the Tyrrhenian Sea, derived from (**left**) DUACS-OI multi-mission altimetry and (**right**) MIOST-K wide-swath altimetry. Vectors represent the magnitude and direction of the geostrophic currents.

MIOST-K shows sharper ADT gradients and stronger velocities than DUACS-OI, with a narrower representation of the boundary flow and finer depiction of mesoscale and finer-scale structures.

The enhanced sharpness and persistence of coastal jets and frontal structures during winter suggest an intensified role of mesoscale and finer-scale dynamics in driving coastal exchanges and vertical mixing. These processes likely contribute to enhanced redistribution of heat and tracers during the winter circulation regime, which is not fully captured by conventional altimetry products.

In the western TYS, near the Strait of Bonifacio, both products capture the wind-induced dipolar circulation, but MIOST-K depicts it with finer spatial detail, revealing smaller eddies and more pronounced shear zones.

Similarly, the central cyclonic gyre shows more spatially structured circulation, with sharper fronts and increased mesoscale variability. The basin-wide coherence of winter sea-level variability observed across tide gauge records is consistent with the winter circulation patterns inferred from altimetry.

Overall, the higher-resolution product provides a finer spatial representation of basin-scale circulation, capturing mesoscale and finer-scale features that are less evident in conventional altimetry.

These differences are particularly marked in coastal regions, where the enhanced resolution enables a more detailed representation of narrow boundary currents and frontal instabilities. This emphasizes how winter mesoscale and finer-scale activity interacts with coastal topography and wind forcing to shape local circulation and mixing.

In winter, the mean surface velocity is 0.097 m/s in DUACS-OI and 0.098 m/s in MIOST-K (+0.9%). The mean ADT gradient is slightly higher in SWOT-enhanced altimetry

(+4.2%), while minimum and maximum ADT values differ by 0.3% and 4.9%, respectively. Spatial variability of velocity (Standard Deviation) is also slightly enhanced in MIOST-K (+7.2%), reflecting sharper fronts and finer-scale structures.

4.2.2. Spring Circulation

During spring, both altimetry products consistently show the basin-wide cyclonic circulation, though with weaker intensity compared to winter (Figure 4). Along the Italian coastline, the northward-flowing current is observed, extending from the Sicily Channel up to the northern TYS, and partially exiting through the Corsica Channel.

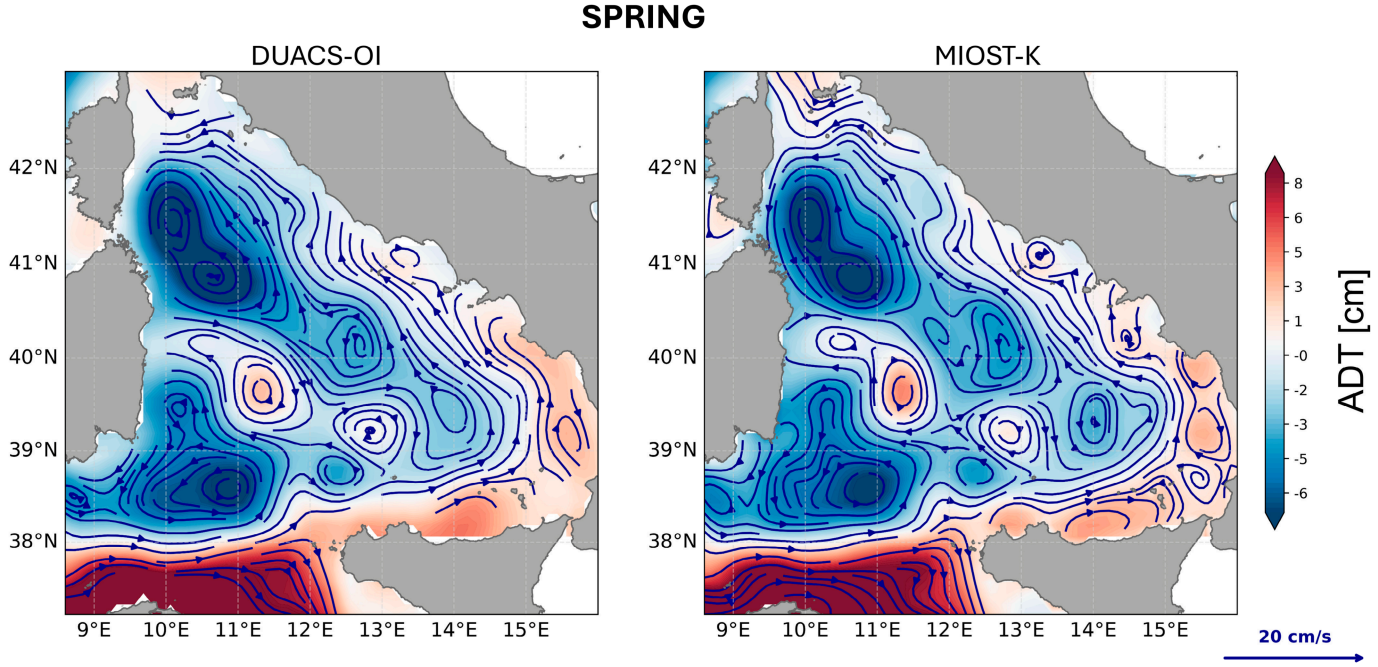


Figure 4. Seasonal mean Absolute Dynamic Topography (ADT) and geostrophic velocity fields for spring in the Tyrrhenian Sea, derived from (**left**) DUACS-OI multi-mission altimetry and (**right**) MIOST-K wide-swath altimetry. Vectors represent the magnitude and direction of the geostrophic currents.

In the high-resolution observations from MIOST-K fields, this boundary current appears sharper and more confined, with higher ADT gradients and stronger velocity vectors than in DUACS-OI, where the signal is more extended and diffuse. Tide gauge records (Figure 3) indicate sustained but reduced coastal sea-level anomalies during spring, consistent with reduced coastal sea-level anomalies during spring compared to winter. In the western TYS, the wind-driven dipolar circulation near the Strait of Bonifacio persists, though less energetic than in winter. SWOT-enhanced altimetry reveals additional small-scale vortices and finer-scale structures embedded within the wind-driven dipolar system, providing new insight into how the transition from winter to spring modulates mesoscale variability and frontal activity, with implications for localized mixing and heat or nutrient redistribution.

Similarly, the central basin cyclonic gyre remains present but appears weaker and less pronounced in DUACS-OI, while MIOST-K shows enhanced mesoscale variability with clearer ADT gradients and finer-scale features. The seasonal evolution inferred from altimetry is temporally consistent with the springtime sea-level variability observed at tide gauge stations across the TYS. The higher resolution of the MIOST-K continues to provide a finer representation of narrow boundary currents, frontal instabilities, and

mesoscale structures that are only partially captured by the conventional DUACS-OI product, providing a more detailed representation of the seasonal transition.

During spring, the mean surface velocity is 0.083 m/s in DUACS-OI and 0.085 m/s in MIOST-K, corresponding to a modest 2.1% increase in the SWOT-enhanced product. The mean ADT gradient is slightly higher in MIOST-K (+6.2%), indicating sharper frontal structures. Minimum and maximum ADT values differ by −1.3% and 3.7%, respectively, while the spatial variability of velocity (standard deviation) increases from 0.056 m/s in DUACS-OI to 0.059 m/s in MIOST-K (+3.8%), indicating a modest increase in the representation of small-scale variability by the higher-resolution product.

4.2.3. Summer Circulation

During summer, the cyclonic circulation weakens considerably (Figure 5). Along the Italian coast, the northward-flowing boundary current remains detectable but weaker, especially north of the Sicily Channel. In the high-resolution fields, this current retains sharper ADT gradients and a more confined path, whereas in DUACS-OI, it appears more diffuse and less intense, often merging with surrounding mesoscale structures.

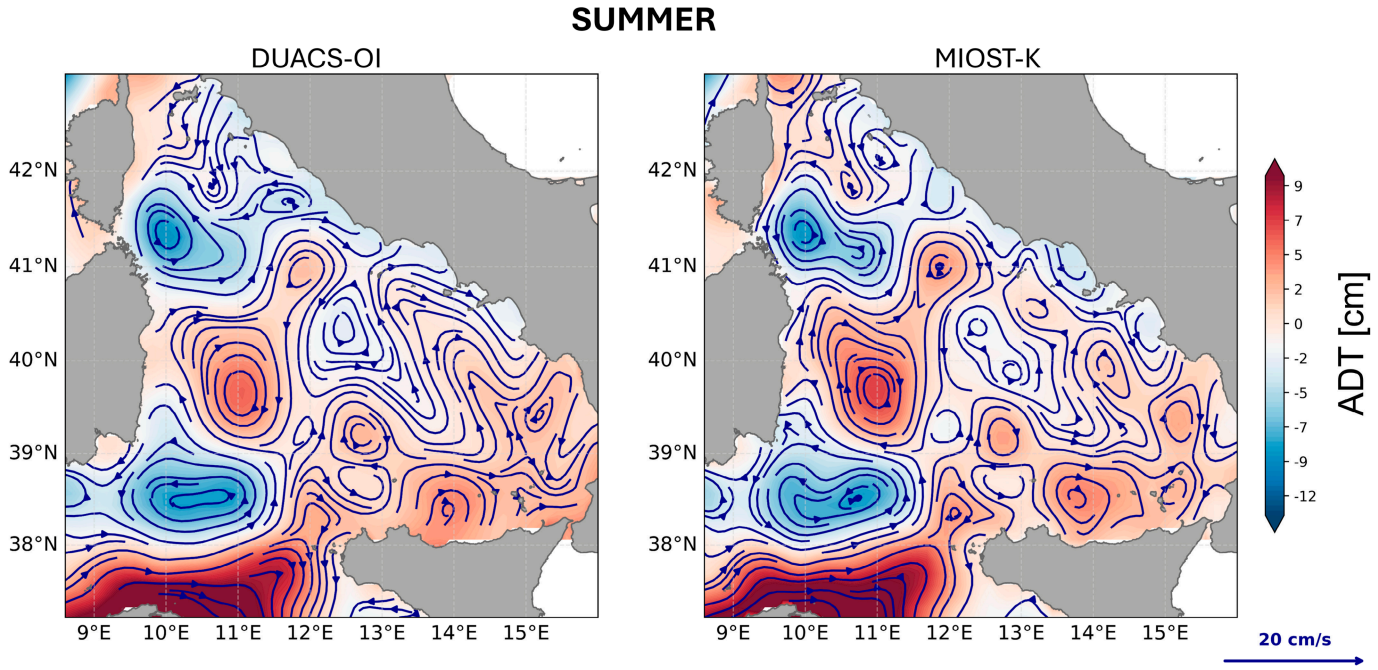


Figure 5. Seasonal mean Absolute Dynamic Topography (ADT) and geostrophic velocity fields for summer in the Tyrrhenian Sea, derived from (**left**) DUACS-OI multi-mission altimetry and (**right**) MIOST-K wide-swath altimetry. Vectors represent the magnitude and direction of the geostrophic currents.

This seasonal weakening is consistent with reduced sea-level variability recorded at tide gauge stations (Figure 3), which show lower-amplitude coastal anomalies during summer. In the western TYS, the wind-driven dipolar circulation near the Strait of Bonifacio becomes less pronounced, yet MIOST-K still depicts finer eddy-like structures and frontal instabilities within the area. These features reveal that, even during the weak summer circulation, coastal and mesoscale processes continue to drive local mixing and influence heat and nutrient distribution, highlighting additional spatial detail during summer. The central basin cyclonic gyre also weakens considerably during summer. In DUACS-OI, it is only faintly discernible, while in MIOST-K, it remains more clearly expressed through enhanced mesoscale variability, including small vortices and localized frontal zones, particularly near the coasts. Moderate but coherent summer sea-level fluctuations observed at

tide gauges support the presence of weak but coherent sea-level variability during summer. Overall, summer circulation is weaker and less organized than in the previous seasons. In this context, MIOST-K provides a more detailed spatial representation of the surface flow, revealing finer-scale frontal structures, localized filaments, and small eddy-like features that are partially smoothed in the DUACS-OI fields.

The quantitative diagnostics indicate overall consistency between the two products, while highlighting subtle differences in the representation of small-scale features. The mean surface velocity is 0.087 m s^{-1} in DUACS-OI and 0.092 m s^{-1} in MIOST-K, corresponding to a 5.7% increase in the SWOT-enhanced product. The mean ADT gradient is slightly higher in MIOST-K (+12.6%), indicating sharper frontal structures. Minimum and maximum ADT values differ by 7.3% and −4.9%, respectively.

In contrast, the spatial variability of velocity (standard deviation) shows a very small decrease from 0.065 m s^{-1} in DUACS-OI to 0.064 m s^{-1} in MIOST-K (−1.6%). This suggests that the two products exhibit comparable bulk variability, while differences are mainly associated with a redistribution of kinetic energy across spatial scales rather than an overall increase in variability.

4.2.4. Autumn Circulation

During autumn, both products show a transition from the weakened summer pattern toward a reorganization of the basin-scale cyclonic regime (Figure 6). Along the Italian coast, the northward boundary current strengthens compared to summer, particularly between the Sicily Channel and the central TYS, although its continuity remains intermittent. In the MIOST-K fields, this current is characterized by sharper ADT gradients and exhibits localized accelerations near the Strait of Messina and other coastal promontories, whereas in DUACS-OI, it appears smoother and less coherent. Tide gauge records (Figure 2) are consistent with increasing coastal sea-level anomalies during autumn.

In the western TYS, the dipolar circulation associated with wind forcing near the Strait of Bonifacio becomes more evident than in summer. While both MIOST-K and DUACS-OI capture the large-scale dipole, MIOST-K additionally resolves embedded eddy-like structures and frontal instabilities, which are largely smoothed in the broader patterns depicted by DUACS-OI. MIOST-K additionally represents embedded mesoscale and finer-scale structures within the wind-driven dipolar circulation, highlighting the reactivation of coastal and basin-scale circulation after summer stratification. These observations provide new insight into the autumn dynamics of the TYS, including the re-establishment of frontal activity, enhanced mixing, and mesoscale variability that are less clearly represented by conventional altimetry.

The central basin cyclonic gyre also shows signs of further intensification, though in DUACS-OI it remains diffuse and difficult to distinguish from the surrounding mesoscale variability. Conversely, MIOST-K shows a more complex mesoscale structure, with multiple mesoscale vortices and narrow frontal zones, particularly in the northern and central TYS. Overall, autumn circulation is characterized by a strengthening of the basin-scale cyclonic regime compared to summer, accompanied by intensified mesoscale activity. MIOST-K provides a more detailed representation of autumn circulation, revealing small-scale eddies and coastal variability that are less resolved in DUACS-OI. During autumn, the mean surface velocity is 0.100 m/s in DUACS-OI and 0.114 m/s in MIOST-K, corresponding to a 14.4% increase in the SWOT-enhanced product. The mean ADT gradient is slightly higher in MIOST-K (+15.0%), reflecting sharper frontal structures. Minimum and maximum ADT values differ by 2.3% and 23.6%, respectively, while the spatial variability of velocity (standard deviation) increases from 0.070 m/s in DUACS-OI to 0.077 m/s in MIOST-K

(+9.7%), indicating increased mesoscale and finer-scale variability captured by the higher-resolution product.

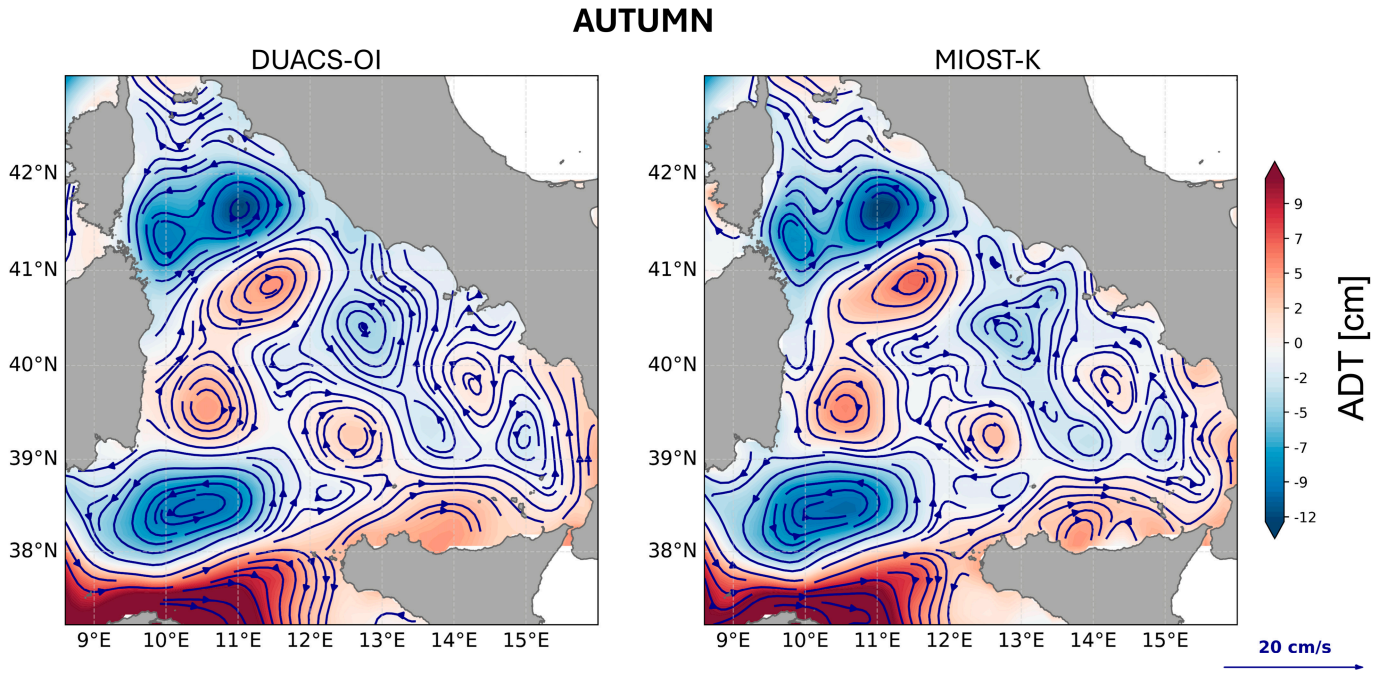


Figure 6. Seasonal mean Absolute Dynamic Topography (ADT) and geostrophic velocity fields for autumn in the Tyrrhenian Sea, derived from (**left**) DUACS-OI multi-mission altimetry and (**right**) MIOST-K wide-swath altimetry. Vectors represent the magnitude and direction of the geostrophic currents.

Across all seasons, the enhanced representation of narrow currents, frontal systems, and eddy activity suggests that fine-scale circulation features are more extensively represented than in conventional gridded altimetry. A concise seasonal synthesis of the quantitative differences between DUACS-OI and MIOST-K across all circulation diagnostics is provided in Table S2. The reported percentage differences are descriptive metrics intended to summarize the relative differences between the two products. As no formal statistical significance test was performed, these values should not be interpreted as evidence of statistically significant differences.

4.3. Comparison with Sea Surface Temperature Observations

To further assess the consistency of the altimetry-derived circulation, we compare ADT fields with contemporaneous SST maps. Thermal gradients at the ocean surface delineate frontal zones and mesoscale structures, providing an independent qualitative reference for assessing the spatial consistency of the altimetry-derived circulation.

SWOT L3 velocity magnitude and SSHA fields are also used to qualitatively assess the dynamical consistency between altimetric observations and SST-derived thermohaline patterns at mesoscale and finer-scale scales.

This comparison allows a qualitative assessment of the spatial coherence between SST gradients, ADT fields, and SWOT L3 structures. Representative cloud-free days are selected for each season to ensure reliable SST coverage.

On 12 January (Figure 7a), the SST distribution reveals the presence of a meridional gradient across the Tyrrhenian basin, with colder waters (~13–14 °C) in the northwestern sector and relatively warmer conditions (~16–17 °C) in the southern and coastal regions. A prominent thermal front extends along the western margin near 10–11° E, indicative of strong horizontal gradients in winter conditions and interaction between open-sea and

coastal waters. This configuration is consistent with winter cyclonic circulation patterns characterized by strong horizontal gradients and mesoscale activity. The ADT (Figure 7b,c) fields show a circulation pattern consistent with the SST distribution, though with clear differences between the two altimetry products. MIOST-K (Figure 7b) provides a finer depiction of sharper and more coherent mesoscale structures, including an anticyclonic eddy centered near 40°N, tightly aligned with the SST front and evident through closely spaced isolines. In contrast, DUACS-OI (Figure 7c) depicts the same region with broader, smoother gradients, with less clearly resolved eddy structures. These differences are consistent with the higher spatial resolution of the SWOT-enhanced product.

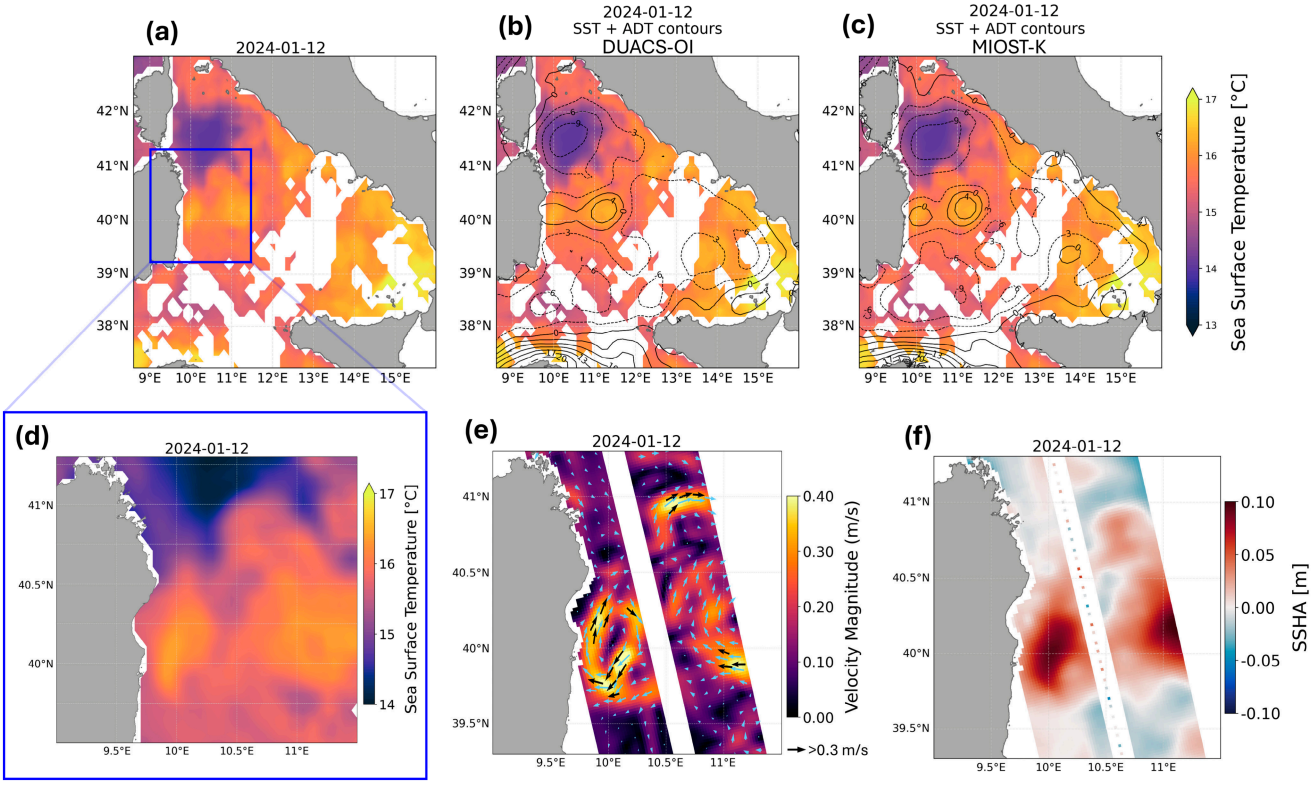


Figure 7. (**a**) SST map; (**b**) SST overlaid with ADT contours from DUACS-OI; (**c**) SST overlaid with ADT contours from MIOST-K; (**d**) zoomed view of the Tyrrhenian Sea; (**e**) geostrophic velocity magnitude, with vectors indicating current direction and magnitude and (**f**) Sea Surface Height Anomaly (SSHA) fields from the SWOT L3 product (track 236, cycle 09). The figure illustrates the spatial correspondence between SST frontal gradients, ADT-derived mesoscale features, and fine-scale dynamical structures resolved by SWOT.

A zoom over the western TYS (Figure 7d) provides additional qualitative evidence from SWOT L3 observations (Figure 7e,f). The SSHA from the SWOT L3 product displays alternating positive and negative patterns of up to ±0.1 m, delineating the eddy periphery and clearly distinguishing its anticyclonic nature. The associated velocity magnitude field derived from SWOT L3 reaches values of 0.4 m s^{-1}, indicating strong velocity gradients around the eddy periphery. This spatial correspondence is consistent with qualitative agreement among SST gradients, ADT fields, and SWOT L3 observations.

These results suggest that SWOT-derived products show a more detailed representation of mesoscale and finer-scale variability compared to conventional gridded altimetry in this case study.

On 4 April, the SST field (Figure 8a) shows a clear meridional thermal contrast in the southern TYS, with temperatures ranging from ~16 °C in the west to ~18 °C along the Sicilian coast. This pattern indicates the early stages of seasonal stratification and

the presence of an active frontal zone extending zonally between 38°N and 39°N. Such thermal gradients coincide with frontal zones and mesoscale variability along the southern boundary of the basin.

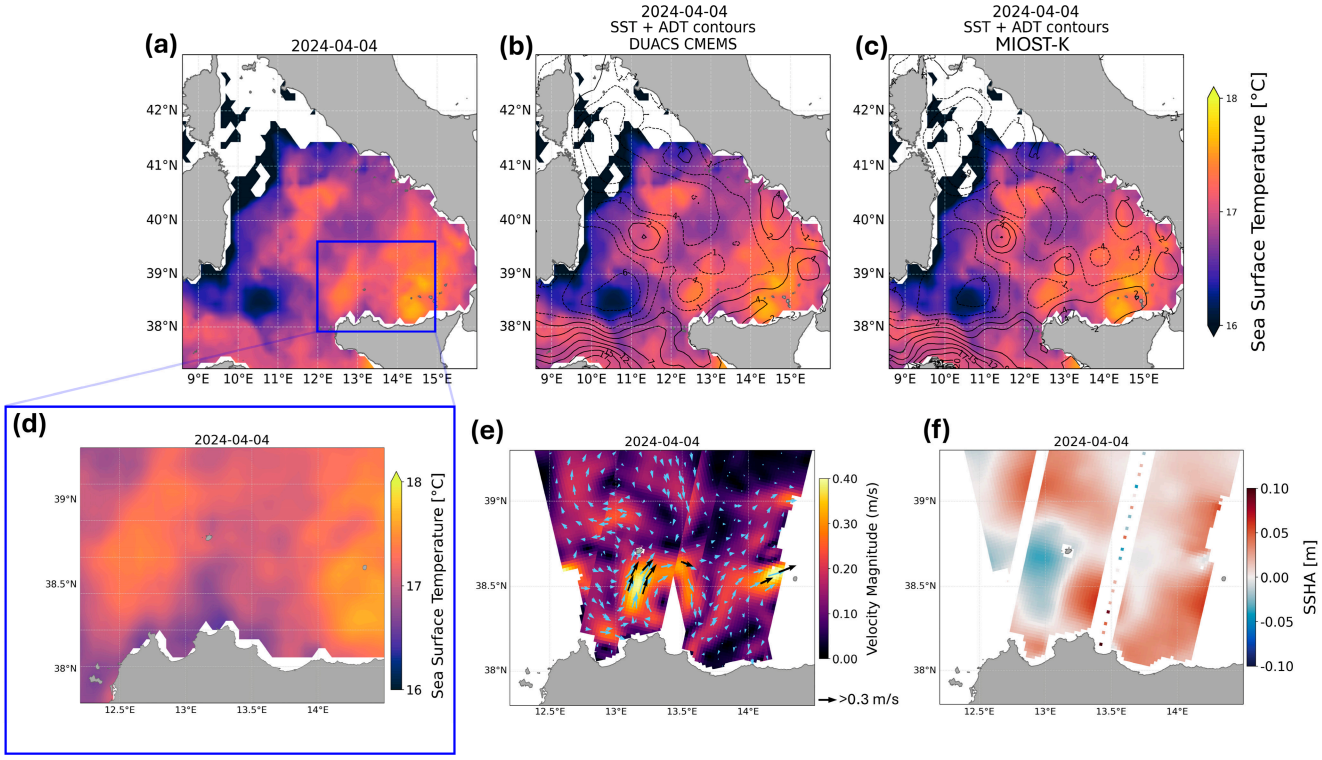


Figure 8. (**a**) SST map; (**b**) SST overlaid with ADT contours from DUACS-OI; (**c**) SST overlaid with ADT contours from MIOST-K; (**d**) zoomed view of the Tyrrhenian Sea; (**e**) geostrophic velocity magnitude, with vectors indicating current direction and magnitude and (**f**) Sea Surface Height Anomaly (SSHA) fields derived from the SWOT L3 product (track 208 and 223, cycle 13). The figure illustrates the spatial correspondence between SST frontal gradients, ADT-derived mesoscale features, and fine-scale dynamical structures resolved by SWOT.

The ADT fields reveal that MIOST-K represents these mesoscale features with enhanced sharpness compared to DUACS-OI. In the MIOST-K map, the ADT isolines delineate a cyclonic structure centered around 13° E, aligned with the SST front, while DUACS-OI provides a smoother representation with reduced frontal intensity and curvature (Figure 8b,c). This suggests that MIOST-K shows sharper mesoscale structures compared to DUACS-OI. A zoom over the southern TYS (Figure 8d) is consistent with SWOT L3 observations (Figure 8e,f). The SSHA field exhibits alternating positive and negative anomalies of up to ± 0.1 m near 13° E, associated with enhanced geostrophic velocities exceeding 0.3 m s^{-1} along the frontal interface. These velocity filaments closely follow the SST gradient and the eddy signatures visible in MIOST-K, indicating strong velocity gradients along the frontal interface. The spatial correspondence among SST gradients, SSH anomalies, and velocity filaments is consistent with the frontal circulation identified in the MIOST-K fields.

Overall, the April case highlights the good qualitative agreement among the SST field, the SWOT L3 observations, and the MIOST-K gridded product, supporting the capability of SWOT-derived products to represent mesoscale and finer-scale dynamics in coastal regions. In contrast, DUACS-OI captures the basin-scale circulation but fails to reproduce the fine-scale frontal complexity evident in the southern TYS.

On 18 July (Figure 9a), the SST field exhibits the typical summer stratification pattern, with surface temperatures exceeding 29–30 °C along the eastern Tyrrhenian coast and slightly cooler waters (~27 °C) in the western and northwestern sectors. The strong zonal

gradient delineates a basin-scale thermal front separating highly stratified, warm waters from relatively cooler, upwelled regions along the western boundary. This configuration is consistent with the mid-summer weakening of the cyclonic basin circulation and the dominance of thermally driven processes at the surface. The altimetric fields are consistent with this regime, but notable differences exist between the products (Figure 9b,c). DUACS-OI presents smoother and more diffuse ADT isolines, with less evident finer structures, and underrepresents mesoscale variability. By contrast, MIOST-K provides a finer depiction of mesoscale features, with closed ADT contours tightly aligned with the SST frontal zone. The enhanced resolution of MIOST-K shows a more detailed mesoscale structure of the summer mesoscale field, consistent with the frontal gradients traced by SST. A zoom over the western TYS (Figure 9d) is consistent with SWOT L3 observations (Figure 9e,f). The SSHA field shows alternating positive and negative anomalies of ± 0.1 m, corresponding to the eddy pair identified in MIOST-K, with associated velocity magnitudes exceeding 0.3 m s^{-1} along the thermal front. Despite the weaker large-scale dynamics, SWOT L3 observations show localized jets and finer-scale vortices that are less evident in DUACS-OI.

Overall, the July snapshot shows a thermally stratified summer surface layer with mesoscale and finer-scale variability. MIOST-K resolves mesoscale and finer-scale structures superimposed on the stratified background, while DUACS-OI provides a smoother, basin-scale depiction of the weakened summer circulation. Strong spatial coherence is observed between the SST front and SWOT-derived anomalies, with fine-scale circulation features present under strongly stratified conditions.

On 30 October (Figure 10a), the SST distribution reveals a well-defined zonal thermal gradient across the northwestern Tyrrhenian basin, with colder waters (≈20–21 °C) along the western offshore sector and progressively warmer conditions (≈23–24 °C) toward the eastern and southern regions. This configuration indicates the late-autumn transition, during which surface cooling and enhanced vertical mixing begin to weaken the summer stratification, especially along the western boundary. The sharp SST gradient between 10° E and 12° E suggests an active frontal zone associated with mesoscale variability.

The ADT fields (Figure 10b,c) show a coherent cyclonic circulation along the western boundary and an anticyclonic structure to the southeast. The MIOST-K product represents these mesoscale systems with greater sharpness and curvature than DUACS-OI, whose smoother fields show smoother gradients and reduced intensity of mesoscale structures. In MIOST-K, the closed ADT isolines near 41°N, 11°E align closely with the SST front, marking the periphery of an eddy structure. These differences are consistent with the finer spatial representation provided by the SWOT-enhanced gridded product.

The zoomed view of the northwestern TYS (Figure 10d) indicates the persistence of the offshore cold filament, where SWOT L3 (Figure 10e,f) shows consistent mesoscale patterns. The SSHA field shows alternating positive and negative anomalies up to ± 0.1 m, consistent with the cyclonic-anticyclonic dipole inferred from the gridded altimetry. Corresponding surface velocities exceed 0.3 m s^{-1} along the eddy rims and frontal boundaries, outlining narrow jets and shear zones that match the SST gradient.

Overall, this October snapshot captures the early autumn evolution of the TYS circulation, characterized by strong horizontal gradients and marked mesoscale activity along the western boundary. The close agreement among the SST front, MIOST-K ADT fields, and SWOT L3 observations supports the qualitative spatial consistency among the three independent datasets.

Although SST gradients and SWOT L3 observations do not provide a direct quantitative validation of the gridded products, their consistent spatial correspondence with the MIOST-K fields across all seasonal case studies provides independent qualitative support for the interpretation of the resolved circulation patterns.

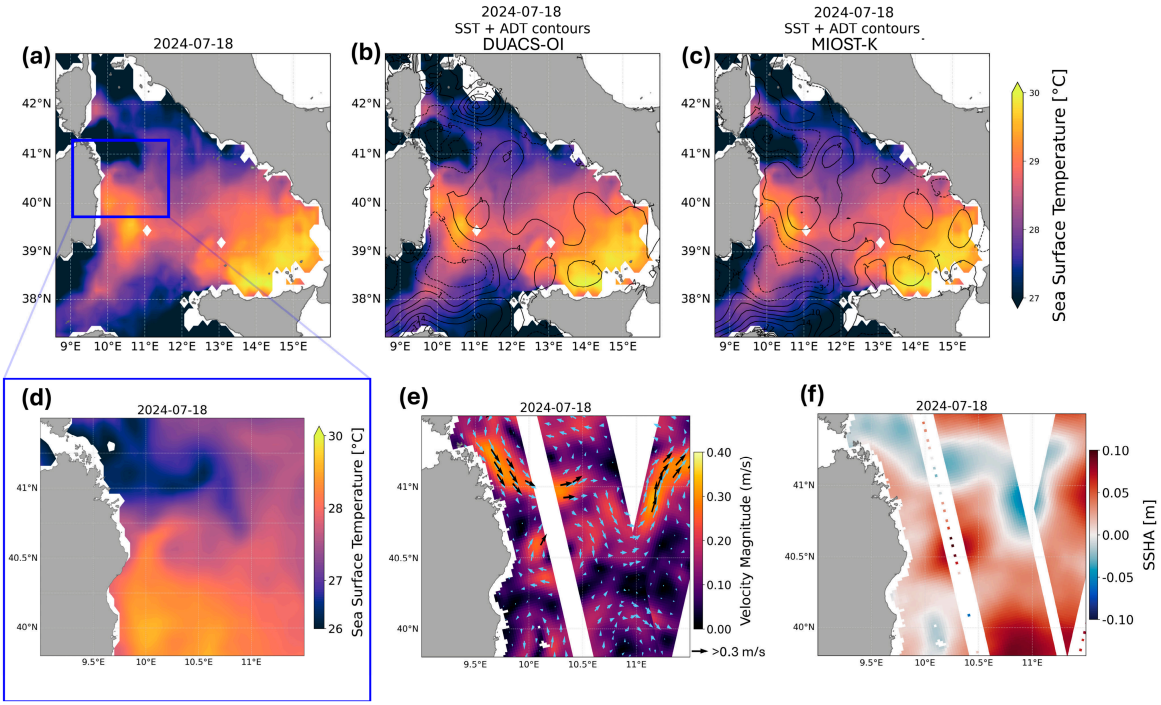


Figure 9. (**a**) SST map; (**b**) SST overlaid with ADT contours from DUACS-OI; (**c**) SST overlaid with ADT contours from MIOST-K; (**d**) zoomed view of the Tyrrhenian Sea; (**e**) geostrophic velocity magnitude, with vectors indicating current direction and magnitude and (**f**) Sea Surface Height Anomaly (SSHA) fields derived from the SWOT L3 product (track 236 and 251, cycle 18). The figure illustrates the spatial correspondence between SST frontal gradients, ADT-derived mesoscale features, and fine-scale dynamical structures resolved by SWOT.

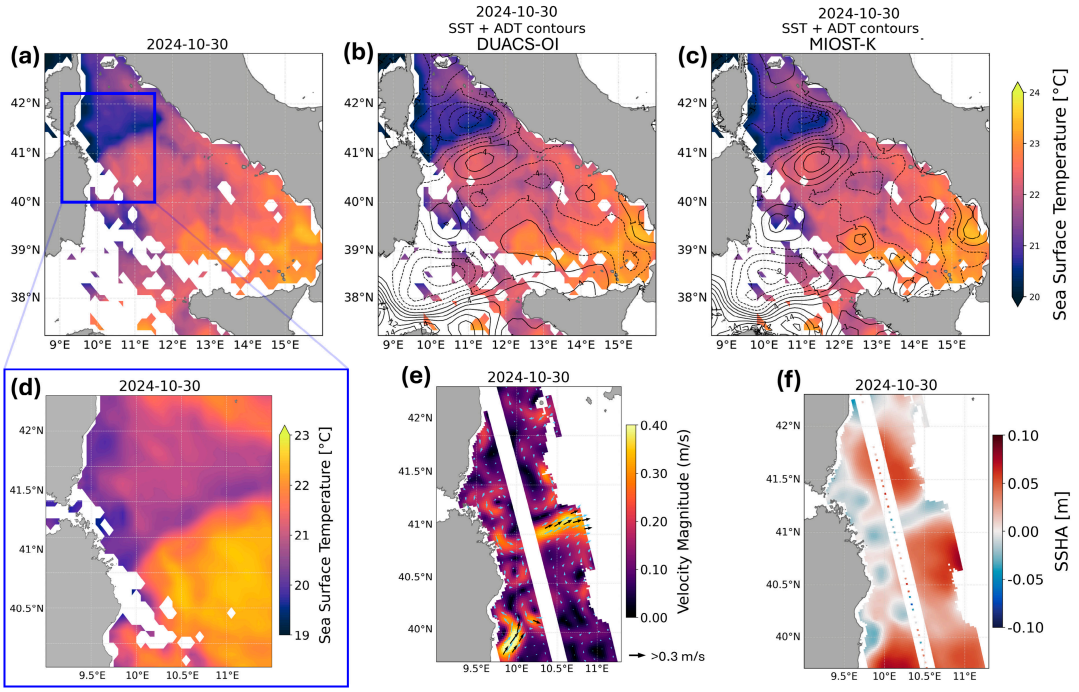


Figure 10. (**a**) SST map; (**b**) SST overlaid with ADT contours from DUACS-OI; (**c**) SST overlaid with ADT contours from MIOST-K; (**d**) zoomed view of the Tyrrhenian Sea; (**e**) geostrophic velocity magnitude, with vectors indicating current direction and magnitude and (**f**) Sea Surface Height Anomaly (SSHA) fields derived from the SWOT L3 product (track 236, cycle 23). The figure illustrates the spatial correspondence between SST frontal gradients, ADT-derived mesoscale features, and fine-scale dynamical structures resolved by SWOT.

5. Discussion

This study investigates the seasonal and coastal surface circulation of the TYS using SWOT-enhanced wide-swath altimetry, in combination with conventional multi-mission altimetry, satellite-derived SST, and coastal tide gauge observations. The analysis provides new observational insight into both basin-scale and fine-scale circulation, particularly in coastal and boundary regions where traditional observations have been limited.

The results confirm the well-established basin-scale cyclonic circulation of the TYS, which intensifies during winter-spring and weakens in summer. Beyond this large-scale pattern, fine-scale circulation features, including narrow boundary currents, persistent coastal jets, sharp frontal structures, and mesoscale vortices, are consistently observed in the altimetry-derived fields and exhibit marked seasonal modulation. These features are particularly evident in coastal and island-dominated regions, where conventional nadir altimetry tends to smooth narrow currents and frontal variability.

Comparisons with independent tide gauge records and satellite SST fields support the consistency of sea-level variability (tide gauges) and surface thermal gradients (SST), respectively, while tide gauges are not used to validate circulation structures such as jets or eddies. SWOT-enhanced products generally exhibit higher correlations and lower RMSE than conventional multi-mission altimetry, consistent with higher spatial resolution and improved representation of coastal variability. The combined use of SWOT L3 and wide-swath gridded products supports the interpretation of mesoscale circulation features in complex coastal environments. SWOT L3 is used exclusively for qualitative inspection of selected case studies and is not included in quantitative seasonal composites or statistical intercomparisons.

Several limitations remain, including the partial smoothing of rapid meteorologically driven sea-level responses and the limited representation of high-frequency coastal processes. These issues highlight the need for longer time series, improved mapping strategies, and integration with complementary in situ and modeling approaches to fully exploit SWOT observations.

It is important to note that the present analysis focuses mainly on L4 gridded products. Because current gridding methods and validation data are limited, this study is likely to capture only part of the information provided by SWOT observations due to current mapping approaches. While the analysis mainly concentrates on geostrophic circulation, SWOT can also observe finer-scale dynamics, such as nonlinear eddies or surface waves, that nadir altimeters and existing mapping approaches cannot resolve. As a result, part of the SWOT signal may not be fully represented in current mapped fields. This underscores the need for new mapping strategies, whether data- or model-driven [53–56], to fully exploit SWOT's submesoscale capabilities.

6. Conclusions

This study is consistent with the well-established basin-scale cyclonic circulation of the TYS, which is stronger in winter-spring and weaker in summer.

Beyond this large-scale pattern, SWOT-enhanced altimetry provides a more detailed spatial representation of coastal and mesoscale variability, suggesting the presence of narrow boundary currents, coastal jet-like features, and frontal structures that are less clearly depicted by conventional multi-mission altimetry.

The combined analysis of SWOT altimetry and satellite SST fields provides qualitative spatial correspondence between surface thermal gradients and mesoscale sea-level structures. Tide gauge observations are used exclusively as an independent reference for assessing sea-level variability, rather than as a direct constraint on circulation features.

Overall, these findings highlight the potential of SWOT for enhancing the characterization of mesoscale and coastal variability in semi-enclosed basins such as the TYS, while also suggesting the need for further investigations to assess the temporal robustness of these features across longer records and independent datasets.

Supplementary Materials: The following supporting information can be downloaded at: https://www.mdpi.com/article/10.3390/rs18142346/s1, Table S1. Pearson correlation coefficients between tide-gauge sea surface height anomalies and the Level-4 altimetry products (MIOST-K and DUACS-OI) before and after applying the optimal temporal lag identified by the cross-correlation analysis. Table S2. Seasonal percentage differences between DUACS-OI and MIOST-K for key circulation diagnostics, including mean surface velocity, mean Absolute Dynamic Topography (ADT) gradient magnitude, minimum and maximum ADT, and spatial standard deviation of velocity magnitude. Percentage differences are computed with respect to DUACS-OI, used as the reference dataset.

Author Contributions: Conceptualization, L.F., Y.C. and G.A.; methodology, L.F., Y.C. and G.A.; software, L.F.; validation, L.F.; formal analysis, L.F.; data curation, L.F.; writing—original draft preparation, L.F.; writing—review and editing, L.F., G.A., M.B., G.F., B.B., A.P. and Y.C.; supervision, Y.C. All authors have read and agreed to the published version of the manuscript.

Funding: This study was carried out within the project "INVMED—Investigation of the intrinsic variability of the Mediterranean Sea" (Project code: 2022CH7P3H; CUP: I53C24002660006), funded by the European Union—NextGenerationEU, under the National Recovery and Resilience Plan (NRRP), Mission 4, Component 2, Investment 1.1—Call for tender No. 104 published on 2 February 2022 by the Italian Ministry of University and Research (MUR). This research was supported by Laura Fortunato's PhD grant in the "Environmental Phenomena and Risks" doctoral program at the University Parthenope of Naples, funded by the PNRR, Mis-sion 4, Component 1, Investment 3.4 "Enhancement of educational services: from nurseries to universities" and Investment 4.1 "University teaching and advanced skills", as well as "Extension of the number of PhD programs and innovative PhDs for public administration and cultural her-itage." This PhD grant was funded under Ministerial Decree No. 351/2022, CUP I61I22000080007. This study has received funding from the Spanish Ministry of Science, Innovation, and Universities, the Spanish Research Agency, the European Regional Development Fund (MCIN/AEI/10.13039/501100011033/FUE) under Grant PID2021-122417NB-I00 (FaSt-SWOT project).

Data Availability Statement: Datasets used in this study are publicly available. Conventional satellite altimetry data were obtained from the Copernicus Marine Environment Monitoring Service (CMEMS) through the Level-4 product SEALEVEL_EUR_PHY_L4_NRT_008_060 (https://doi.org/10.48670/moi-00142). Sea surface temperature data were obtained from CMEMS under product SST_MED_PHY_L3S_MY_010_042 (https://doi.org/10.48670/moi-00314). SWOT-enhanced altimetry data, including the experimental Level-4 MIOST product and the Expert Level-3 Low-Rate Sea Surface Height dataset, were retrieved from AVISO+ (https://doi.org/10.24400/527896/A01-2024.007). Tide gauge data from Palermo, Marina di Campo, and Ginostra are available from the ISPRA National Tide Gauge Network (Rete Mareografica Nazionale, RMN) and can be accessed via the ISPRA portal (www.mareografico.it). The Solenzara tide gauge dataset is available through the SONEL repository (https://www.sonel.org). The Ischia tide gauge dataset can be requested from the corresponding author upon reasonable request. Custom scripts used for data preprocessing and analysis are available from the corresponding author upon reasonable request.

Acknowledgments: The authors would like to thank the project "Un approccio multidisciplinare alla contaminazione da idrocarburi nei mitili allevati nel Golfo di Pozzuoli," supported by the University of Naples Parthenope Local Research Project 2023, in which some of the authors are involved. Gratitude is also extended to the European Union—NextGenerationEU, National Recovery and Resilience Plan (PNRR), Mission 4, Component 2, Investment 1.4, "Strengthening research infrastructures and creation of national R&D sample centers on selected Key Enabling Technologies," Code CN00000023—Sustainable Mobility Center (Centro Nazionale per la Mobilità Sostenibile—CNMS), Spoke 3 "Waterways" and Spoke 7 "CCAM, Connected Networks and Smart Infrastruc-ture," in

which some of the authors also participate. The authors also acknowledge the Antarctic Circumpolar Current Eddies Survey and Simulations (ACCESS) project (PNRA 19_00032), part of the Italian National Antarctic Research Program (PNRA), with the authors' involvement.

Conflicts of Interest: Author Maxime Ballarotta was employed by the company Collecte Localisation Satellites (CLS). The remaining authors declare that the research was conducted in the absence of any commercial or financial relationships that could be construed as a potential conflict of interest.

Abbreviations

The following abbreviations are used in this manuscript:

TYS	Tyrrhenian Sea
SWOT	Surface Water and Ocean Topography
SST	Sea Surface Temperature
ADT	Absolute Dynamic Topography
RMSE	Root Mean Square Error
SSHA	Sea Surface Height Anomaly
SSH	Sea Surface Height
mAW	Modified Atlantic Water
LIW	Levantine Intermediate Water
WMDW	Western Mediterranean Deep Water
TDW	Tyrrhenian Deep Water
TIW	Tyrrhenian Intermediate Water
L4	Level-4
L3	Level-3

References

1. Krivosheya, V.G.; Ovchinnikov, I.M. Peculiarities in the geostrophic circulation of the waters of the Tyrrhenian Sea. *Oceanology* **1973**, *13*, 822–827.
2. Millot, C. Circulation in the western Mediterranean Sea. *J. Mar. Syst.* **1999**, *20*, 423–442. [CrossRef]
3. Fusco, G.; Manzella, G.M.R.; Cruzado, A.; Gačić, M.; Gasparini, G.P.; Kovačević, V.; Millot, C.; Tziavos, C.; Velasquez, Z.R.; Walne, A.; et al. Variability of mesoscale features in the Mediterranean Sea from XBT data analysis. *Ann. Geophys.* **2003**, *21*, 21–32. [CrossRef]
4. Fusco, G.; Artale, V.; Cotroneo, Y.; Sannino, G. Thermohaline variability of Mediterranean Water in the Gulf of Cadiz, 1948–1999. *Deep. Sea Res. Part I Oceanogr. Res. Pap.* **2008**, *55*, 1624–1638. [CrossRef]
5. Cotroneo, Y.; Aulicino, G.; Ruiz, S.; Pascual, A.; Budillon, G.; Fusco, G.; Tintoré, J. Glider and satellite high resolution monitoring of a mesoscale eddy in the algerian basin: Effects on the mixed layer depth and biochemistry. *J. Mar. Syst.* **2016**, *162*, 73–88. [CrossRef]
6. Astraldi, M.; Gasparini, G.P. The seasonal characteristics of the circulation in the Tyrrhenian Sea. *Seas. Interannual Var. West. Mediterr. Sea* **1994**, *46*, 115–134. [CrossRef]
7. Hopkins, T.S. Recent observations on the intermediate and deep water circulation in the Southern Tyrrhenian Sea. *Oceanol. Acta* **1988**, *9*, 41–50. [CrossRef]
8. Bianchi, C.N.; Morri, C. Marine biodiversity of the Mediterranean Sea: Situation, problems and prospects for future research. *Mar. Pollut. Bull.* **2000**, *40*, 367–376. [CrossRef]
9. Fortunato, L.; Esposito, M.; Capozzi, V.; Conversano, F.; Gifuni, L.; De Ruggiero, P.; Aulicino, G.; Di Luccio, D.; Zambianchi, E.; Budillon, G.; et al. The role of sea surface circulation and weather dynamics in the PAH contamination in coastal mussels: A case study in the Southern Tyrrhenian sea. *Front. Mar. Sci.* **2025**, *12*, 1565042. [CrossRef]
10. Fu, L.L.; Cazenave, A. (Eds.) *Satellite Altimetry and Earth Sciences: A Handbook of Techniques and Applications*; Elsevier: Amsterdam, The Netherlands, 2000; Volume 69.
11. Aulicino, G.; Cotroneo, Y.; Olmedo, E.; Cesarano, C.; Fusco, G.; Budillon, G. In-situ and satellite sea surface salinity in the algerian basin observed through ABACUS glider measurements and BEC SMOS regional products. *Remote Sens.* **2019**, *11*, 1361. [CrossRef]
12. Le Traon, P.Y.; Nadal, F.; Ducet, N. An improved mapping method of multisatellite altimeter data. *J. Atmos. Ocean. Technol.* **1998**, *15*, 522–534. [CrossRef]
13. Pascual, A.; Pujol, M.I.; Larnicol, G.; Le Traon, P.Y.; Rio, M.H. Mesoscale mapping capabilities of multisatellite altimeter missions: First results with real data in the Mediterranean Sea. *J. Mar. Syst.* **2007**, *65*, 190–211. [CrossRef]

14. Abdalla, S.; Kolahchi, A.A.; Ablain, M.; Adusumilli, S.; Bhowmick, S.A.; Alou-Font, E.; Amarouche, L.; Andersen, O.B.; Antich, H.; Aouf, L.; et al. Altimetry for the future: Building on 25 years of progress. *Adv. Space Res.* **2021**, *68*, 319–363. [CrossRef]
15. Fu, L.L.; Alsdorf, D.; Morrow, R.; Rodriguez, E.; Mognard, N. *SWOT: The Surface Water and Ocean Topography Mission. Wide-Swath Altimetric Elevation on Earth*; No. JPL-Publ-12-5; NASA Jet Propulsion Laboratory: Pasadena, CA, USA, 2012.
16. Morrow, R.; Fu, L.-L.; Ardhuin, F.; Benkiran, M.; Chapron, B.; Cosme, E.; D'oVidio, F.; Farrar, J.T.; Gille, S.T.; Lapeyre, G.; et al. Global observations of fine-scale ocean surface topography with the Surface Water and Ocean Topography (SWOT) mission. *Front. Mar. Sci.* **2019**, *6*, 232. [CrossRef]
17. Fu, L.L.; Pavelsky, T.; Cretaux, J.F.; Morrow, R.; Farrar, J.T.; Vaze, P.; Sengenes, P.; Vinogradova-Shiffer, N.; Sylvestre-Baron, A.; Picot, N.; et al. The surface water and ocean topography mission: A breakthrough in radar remote sensing of the ocean and land surface water. *Geophys. Res. Lett.* **2024**, *51*, e2023GL107652. [CrossRef]
18. Fortunato, L.; Gómez-Navarro, L.; Combes, V.; Cotroneo, Y.; Aulicino, G.; Pascual, A. Coastal Eddy Detection in the Balearic Sea: SWOT Capabilities. *Remote Sens.* **2025**, *17*, 2552. [CrossRef]
19. Verger-Miralles, E.; Mourre, B.; Gómez-Navarro, L.; Barceló-Llull, B.; Casas, B.; Cutolo, E.; Díaz-Barroso, L.; D'oVidio, F.; Tarry, D.R.; Zarokanellos, N.D.; et al. SWOT enhances small-scale eddy detection in the Mediterranean Sea. *Geophys. Res. Lett.* **2025**, *52*, e2025GL116480. [CrossRef]
20. Zhang, H.; Fan, C.; Huang, L.; Sun, L.; Meng, J. SWOT-based detection of sea surface height variations induced by internal solitary waves: Feature extraction and amplitude inversion. *IEEE J. Sel. Top. Appl. Earth Obs. Remote Sens.* **2025**, *19*, 805–814. [CrossRef]
21. Turki, E.I.; Islam, M.S.; Lopez Solano, C.; Salameh, E.; Domingues, M.; Mendoza, T.; Aouf, L.; Froideval, L.; Gutierrez Barcelo, D.; Laignel, B.; et al. On the use of SWOT altimetry data for monitoring coastal hydrodynamics. *Int. J. Appl. Earth Obs. Geoinf.* **2025**, *145*, 104982. [CrossRef]
22. Vega-Gimenez, D.; Amores, A.; Paris, A.; Pascual, A. Expanding the coastal observation frontier: SWOT reveals the spatial footprint of storm surges. *Geophys. Res. Lett.* **2025**, *52*, e2025GL117299. [CrossRef]
23. Marani, M.; Gamberi, F.; Bonatti, E. From seafloor spreading to passive margin: Tectonic evolution of the Tyrrhenian Sea. *Mem. Soc. Geol. It.* **1993**, *49*, 373–385.
24. Aulicino, G.; Cotroneo, Y.; Lacava, T.; Sileo, G.; Fusco, G.; Carlon, R.; Satriano, V.; Pergola, N.; Tramutoli, V.; Budillon, G. Results of the first Wave Glider experiment in the southern Tyrrhenian Sea. *Adv. Oceanogr. Limnol.* **2016**, *7*, 16. [CrossRef]
25. de la Vara, A.; Parras-Berrocal, I.M.; Izquierdo, A.; Sein, D.V.; Cabos, W. Climate change signal in the ocean circulation of the Tyrrhenian Sea. *Earth Syst. Dyn.* **2022**, *13*, 303–319. [CrossRef]
26. Millot, C.; Candela, J.; Fuda, J.L.; Tber, Y. Large warming and salinification of the Mediterranean outflow due to changes in its composition. *Deep. Sea Res. Part I Oceanogr. Res. Pap.* **2006**, *53*, 656–666. [CrossRef]
27. Iacono, R.; Napolitano, E.; Marullo, S.; Artale, V.; Vetrano, A. Seasonal variability of the Tyrrhenian Sea surface geostrophic circulation as assessed by altimeter data. *J. Phys. Oceanogr.* **2013**, *43*, 1710–1732. [CrossRef]
28. Durante, S.; Oliveri, P.; Nair, R.; Sparnocchia, S. Mixing in the Tyrrhenian interior due to thermohaline staircases. *Front. Mar. Sci.* **2021**, *8*, 672437. [CrossRef]
29. Astraldi, M.; Gasparini, G.P.; Vetrano, A.; Vignudelli, S. Hydrographic characteristics and interannual variability of water masses in the central Mediterranean: A sensitivity test for long-term changes in the Mediterranean Sea. *Deep. Sea Res. Part I Oceanogr. Res. Pap.* **2002**, *49*, 661–680. [CrossRef]
30. Poulain, P.M.; Zambianchi, E. Surface circulation in the central Mediterranean Sea as deduced from Lagrangian drifters in the 1990s. *Cont. Shelf Res.* **2007**, *27*, 981–1001. [CrossRef]
31. Millot, C. Circulation in the western Mediterranean-sea. *Oceanol. Acta* **1987**, *10*, 143–149.
32. Astraldi, M.; Gasparini, G.P.; Sparnocchia, S.; Moretti, M.; Sansone, E. The characteristics of the water masses and the water transport in the Sicily Strait at long time scales. *Bull.-Inst. Oceanogr. MONACO-NUMERO Spec.* **1996**, 95–116.
33. Budillon, G.; Gasparini, G.P.; Schroeder, K. Persistence of an eddy signature in the central Tyrrhenian basin. *Deep. Sea Res. Part II Top. Stud. Oceanogr.* **2009**, *56*, 713–724. [CrossRef]
34. Rinaldi, E.; Buongiorno Nardelli, B.; Zambianchi, E.; Santoleri, R.; Poulain, P.M. Lagrangian and Eulerian observations of the surface circulation in the Tyrrhenian Sea. *J. Geophys. Res. Ocean.* **2010**, *115*, C04024. [CrossRef]
35. Iacono, R.; Napolitano, E.; Palma, M.; Sannino, G. The tyrrhenian sea circulation: A review of recent work. *Sustainability* **2021**, *13*, 6371. [CrossRef]
36. Bonaduce, A.; Cipollone, A.; Johannessen, J.A.; Staneva, J.; Raj, R.P.; Aydogdu, A. Ocean mesoscale variability: A case study on the Mediterranean Sea from a re-analysis perspective. *Front. Earth Sci.* **2021**, *9*, 724879. [CrossRef]
37. Durante, S.; Schroeder, K.; Mazzei, L.; Pierini, S.; Borghini, M.; Sparnocchia, S. Permanent thermohaline staircases in the Tyrrhenian Sea. *Geophys. Res. Lett.* **2019**, *46*, 1562–1570. [CrossRef]
38. Sparnocchia, S.; Gasparini, G.P.; Astraldi, M.; Borghini, M.; Pistek, P. Dynamics and mixing of the Eastern Mediterranean outflow in the Tyrrhenian basin. *J. Mar. Syst.* **1999**, *20*, 301–317. [CrossRef]

39. Zodiatis, G.; Gasparini, G.P. Thermohaline staircase formations in the Tyrrhenian Sea. *Deep. Sea Res. Part I Oceanogr. Res. Pap.* **1996**, *43*, 655–678. [CrossRef]
40. Pujol, M.-I.; Faugère, Y.; Taburet, G.; Dupuy, S.; Pelloquin, C.; Ablain, M.; Picot, N. DUACS DT2014: The new multi-mission altimeter data set reprocessed over 20 years. *Ocean Sci.* **2016**, *12*, 1067–1090. [CrossRef]
41. Ubelmann, C.; Dibarboure, G.; Gaultier, L.; Ponte, A.; Ardhuin, F.; Ballarotta, M.; Faugère, Y. Reconstructing ocean surface current combining altimetry and future spaceborne Doppler data. *J. Geophys. Res. Ocean.* **2021**, *126*, e2020JC016560. [CrossRef]
42. Ubelmann, C.; Carrere, L.; Durand, C.; Dibarboure, G.; Faugère, Y.; Ballarotta, M.; Briol, F.; Lyard, F. Simultaneous estimation of ocean mesoscale and coherent internal tide sea surface height signatures from the global altimetry record. *Ocean Sci.* **2022**, *18*, 469–481. [CrossRef]
43. Ballarotta, M.; Ubelmann, C.; Bellemin-Laponnaz, V.; Le Guillou, F.; Meda, G.; Anadon, C.; Laloue, A.; Delepoulle, A.; Faugère, Y.; Pujol, M.-I.; et al. Assimilation of Wide-Swath Altimetry in Level-4 Multi-Mission Satellite Maps. *Ocean Sci.* **2025**, *21*, 63–80. [CrossRef]
44. Buonocore, B.; Cotroneo, Y.; Capozzi, V.; Aulicino, G.; Zambardino, G.; Budillon, G. Sea-level variability in the Gulf of Naples and the "Acqua Alta" episodes in Ischia from tide-gauge observations in the period 2002–2019. *Water* **2020**, *12*, 2466. [CrossRef]
45. Bonaduce, A.; Pinardi, N.; Oddo, P.; Spada, G.; Larnicol, G. Sea-level variability in the Mediterranean Sea from altimetry and tide gauges. *Clim. Dyn.* **2016**, *47*, 2851–2866. [CrossRef]
46. Cipollini, P.; Calafat, F.M.; Jevrejeva, S.; Melet, A.; Prandi, P. Monitoring sea-level in the coastal zone with satellite altimetry and tide gauges. *Integr. Study Mean. Sea-Lev. Its Compon.* **2017**, *38*, 35–59. [CrossRef]
47. Passaro, M.; Juhl, M.C. On the potential of mapping sea-level anomalies from satellite altimetry with Random Forest Regression. *Ocean Dyn.* **2023**, *73*, 107–116. [CrossRef]
48. López-García, P.; Gómez-Enri, J.; Muñoz-Pérez, J.J. Accuracy assessment of wave data from altimeter near the coast. *Ocean Eng.* **2019**, *178*, 229–232. [CrossRef]
49. Risien, C.M.; Strub, P.T. Blended sea-level anomaly fields with enhanced coastal coverage along the US West Coast. *Sci. Data* **2016**, *3*, 160013. [CrossRef]
50. Oelsmann, J.; Passaro, M.; Dettmering, D.; Schwatke, C.; Sánchez, L.; Seitz, F. The zone of influence: Matching sea-level variability from coastal altimetry and tide gauges for vertical land motion estimation. *Ocean Sci.* **2021**, *17*, 35–57. [CrossRef]
51. Pisano, A.; Nardelli, B.B.; Tronconi, C.; Santoleri, R. The new Mediterranean optimally interpolated pathfinder AVHRR SST Dataset (1982–2012). *Remote Sens. Environ.* **2016**, *176*, 107–116. [CrossRef]
52. Embury, O.; Merchant, C.J.; Good, S.A.; Rayner, N.A.; Høyer, J.L.; Atkinson, C.; Block, T.; Alerskans, E.; Pearson, K.J.; Worsfold, M.; et al. Satellite-based time-series of sea-surface temperature since 1980 for climate applications. *Sci. Data* **2024**, *11*, 326. [CrossRef] [PubMed]
53. Le Guillou, F.; Chapron, B.; Rio, M.-H. VarDyn: Dynamical joint reconstructions of sea surface height and temperature from multi-sensor satellite observations. *J. Adv. Model. Earth Syst.* **2025**, *17*, e2024MS004689. [CrossRef]
54. Fablet, R.; Beauchamp, M.; Drumetz, L.; Rousseau, F. Joint Interpolation and Representation Learning for Irregularly Sampled Satellite-Derived Geophysical Fields. *Front. Appl. Math. Stat.* **2021**, *7*, 655224. [CrossRef]
55. Beauchamp, M.; Febvre, Q.; Georgenthum, H.; Fablet, R. 4DVarNet-SSH: End-to-end learning of variational interpolation schemes for nadir and wide-swath satellite altimetry. *Geosci. Model Dev.* **2023**, *16*, 2119–2147. [CrossRef]
56. Martin, S.A.; Manucharyan, G.E.; Klein, P. Synthesizing sea surface temperature and satellite altimetry observations using deep learning improves the accuracy and resolution of gridded sea surface height anomalies. *J. Adv. Model. Earth Syst.* **2023**, *15*, e2022MS003589. [CrossRef]

Disclaimer/Publisher's Note: The statements, opinions and data contained in all publications are solely those of the individual author(s) and contributor(s) and not of MDPI and/or the editor(s). MDPI and/or the editor(s) disclaim responsibility for any injury to people or property resulting from any ideas, methods, instructions or products referred to in the content.